

Multiplexing Precision RVs: Searching for Close in Gas Giants in Open Clusters

John I. Bailey, III¹, Mario Mateo

*Department of Astronomy, University of Michigan
1085 South University, Ann Arbor, MI 48109, USA*

baileyji@umich.edu

Russel J. White

*Department of Physics & Astronomy, Georgia State University
P.O. Box 4106, Atlanta, GA 30302, USA*

Stephen A. Sheckman, Jeffrey D. Crane

*Carnegie Observatories
813 Santa Barbara Street, Pasadena, CA 91101, USA*
and

Edward W. Olszewski

*Steward Observatory
933 North Cherry Avenue, Tucson, AZ 85721, USA*

Abstract

We present a multiplexed, high-resolution ($R \sim 50,000$ median) spectroscopic survey designed to detect exoplanet candidates in two southern star clusters (NGC 2516 and NGC 2422) using the Michigan/Magellan Fiber System (M2FS) on the Magellan/Clay telescope at Las Campanas Observatory. With 128 available fibers in our observing mode, we are able to target every star in the core half-degree of each cluster that could plausibly be a solar-analog member. Our template-based spectral fits provide precise measurements of fundamental stellar properties— T_{eff} (± 30 K), $[Fe/H]$ and $[\alpha/Fe]$ (± 0.02 dex), and $v_r \sin(i)$ (± 0.3 km/s)—and radial velocities (RVs) by using telluric absorption features from 7160 to 7290 Å as a wavelength reference for 251 mid-F to mid-K stars (126 in NGC 2516 and 125 in NGC 2422) that comprise our survey. In each cluster we have obtained $\sim 10 - 12$ epochs of our targets. Using repeat observations of an RV standard star we show our approach can attain a single-epoch velocity precision of 25 m/s to 60 m/s over a broad range of S/N throughout our observational baseline of 1.1 years. Our technique is suitable for non-rapidly rotating stars cooler than mid-F. In this paper we describe our observational sample, analysis methodology, and present a detailed study of the attainable precision and measurement capabilities of our approach. Subsequent papers will provide results for stars observed in the target clusters, analyze our dataset of RV time-series for stellar jitter and stellar and sub-stellar companions, and consider the implications of our findings on the clusters themselves.

Subject headings: methods: data analysis, open clusters and associations: individual (NGC 2516, NGC 2422), techniques: radial velocities, techniques: spectroscopic

1. Introduction

The realization that planetary systems can harbor hot gas giants led to drastic revisions to both theories of planet formation and dynamical evolution. Contemporary formation models typically fall into the broad categories of core accretion (Mizuno et al. 1980) or disk instability models (Boss 1997), neither of which has yet emerged as a dominant driver. It also remains unclear if the orbits of the so-called Hot-Jupiters evolve inward through coupling to a gaseous disk (Goldreich & Tremaine 1980; Lin et al. 1996), via dynamical scattering off clumps and other bodies (e.g., Rasio & Ford 1996; Jurić & Tremaine 2008), or even secular interactions with a distant stellar companion (Kozai cycles; e.g., Fabrycky & Tremaine 2007). Though much effort has been spent testing these theories they all remain viable, at least for some systems (see review by Helled et al. 2014). The core reason is that diagnostics (e.g. the period-eccentricity distribution) are muddled by the wide and often unknown ages of host stars in field star exoplanetary systems. A direct solution would be to find young exoplanets with ages ~ 1 Myr, however the extreme activity of host stars at T Tauri ages has thus far inhibited detecting planets (e.g. Huerta et al. 2008; Huélamo et al. 2008; Prato et al. 2008; Crockett et al. 2012; Bailey et al. 2012); some very young candidates nevertheless remain (e.g. Ciardi et al. 2015).

These theories do make various distinct predictions regarding the properties of hot gas giants and their orbits for the first ~ 1 Gyr (c.f. Adams & Laughlin 2006; Marley et al. 2007; Fortney & Nettelmann 2010; Fortney et al. 2008 vs. Galvagni et al. 2012; but see also Mordasini et al. 2012), and though some constraints require direct measures of properties via transits, which are rare, they are relatively more likely for hot gas giants ($\sim 5\%$ for hot gas giants; Charbonneau et al. 2007). Indeed, considerable effort has been expended searching for such systems with known ages (e.g., Paulson et al. 2004; Bailey et al. 2012). The first exoplanets orbiting solar-like stars in a cluster (F, G, or K and on the main sequence) were announced by Quinn et al. (2012). To date, gas giant exoplanets orbiting main sequence (MS) stars in clusters have been

discovered via transits (NGC 6811 Meibom et al. 2013) and RV techniques (M 67; Brucalassi et al. 2014; Praesepe, Quinn et al. 2012; Hyades, Quinn et al. 2014), though none of the latter are also transiting systems. One system discovered in the Hyades is noteworthy for its distinctly non-zero eccentricity ($e = 0.08 \pm 0.02$), which implies that dynamical scattering has likely played a role in its dynamical evolution, at least in the late stages of the process (Quinn et al. 2014). It is already clear that even a few hot gas giant exoplanets in open clusters with precise ages have the potential to strongly constrain planet-migration theories. Any such systems that also happen to be transiting will produce even more powerful constraints on gas giant formation models by revealing precise information on the sizes, densities and compositions of exoplanets with well-determined ages. Indeed, identifying transiting planets in open clusters is a key science goal of NASA’s K2 mission (Howell et al. 2014).

The practical problem of finding cluster exoplanets is one of efficiency. Over the two decades of exoplanetary searches, more than 600 systems have been studied using RV techniques. In contrast, there are only eight known exoplanets orbiting MS stars in open clusters. The deficiency of known exoplanets in clusters is not a consequence of higher stellar RV jitter. Measured values of this in open clusters are ~ 15 m/s at ~ 400 Myr (Paulson et al. 2004; Quinn et al. 2012), which is roughly an order of magnitude less than the amplitude induced by a typical hot gas giant. Rather, clusters tend to be considerably more distant than the closest individual field stars and are hence fainter and consequently harder to monitor. Moreover the same technique used for field stars – individual spectra, one star at a time – is typical of cluster surveys. Lengthy campaigns involving thousands of visits are needed to find the comparatively rare cases with detectable velocity amplitudes: only $1.2 \pm 0.4\%$ of all FGK stars in the solar neighborhood harbor hot gas giants (Wright et al. 2012) and cluster occurrence rates appear similar (Meibom et al. 2013) so hundreds of targets must be monitored. The MARVELS survey (Ge et al. 2008) is a notable exception to this with its $\sim 11,000$ stars and is intended to attain similar RV precision to the work we report here though it is not targeted to clusters.

¹Current Affiliation: Leiden Observatory, Leiden University, P.O. Box 9513, 2300RA Leiden, The Netherlands

In this paper we introduce a different approach that employs highly-multiplexed RV techniques to detect and study exoplanetary systems containing hot gas giants down to $\sim 0.1 M_{Jup}$ that are orbiting stars in clusters that range in age from about 100 Myr to nearly 1 Gyr. To our knowledge our survey is the first multi-object spectroscopic survey of open cluster stars to obtain RV precisions at the sub-hundred m/s level. To do this, we have used spectra obtained with the Michigan/Magellan Fiber System (M2FS; Mateo et al. 2012) which allows us to obtain multiplexed, high-resolution ($R \sim 50,000$) optical spectra of solar-analogue stars (spectra types F5V to K5V) in nearby ($\lesssim 1$ kpc) clusters. Our approach – a variant of the telluric-reference approach first proposed by Griffin & Griffin (1973) and subsequently used or studied by Cochran (1988, and references therein), Seifahrt et al. (2010), and Bailey et al. (2012) – models the observed stellar spectra and telluric absorption features to obtain high-precision velocities and stellar parameters. As part of this process we map out the RV precision attainable using telluric lines across a wide range of wavelengths and quantify the assertions of Griffin & Griffin (1973) from some 43 years ago. We are able to measure RVs to 25 m/s for a slowly rotating, bright RV standard star and 30–60 m/s for up to 128 stars simultaneously over a half-degree field-of-view. We expect our precision to remain better than ~ 75 m/s for stars as faint as $V = 17$. Though our precision is not particularly notable when compared with e.g. the 0.3 m/s precision of HARPS (Mayor et al. 2003) or similar instruments, it is comparable to the expected performance of MARVELS and our magnitude limit is significantly beyond the survey’s $V=12$ limit. HARPS is capable of 30 m/s precision at $V = 16.6$ but it requires ~ 1 hour exposure – 4000 times less efficient than our multi-object approach.

The goal of this paper is to describe the details of our methodology. We will address the stellar properties and RV variability of our target stars in future publications. We describe our target selection and observing procedure in Section 2. Section 3 describes our image reduction procedure and extraction to 1D spectra. In Section 4 we present our spectral modeling approach and describe the procedure in detail. Section 5 analyzes the quality of the measured RVs and stellar

parameters. Finally Section 6 considers the implications of our results for the future of this survey technique.

2. Observations

2.1. Cluster and Spectroscopic Target Selection

To select our targets, we first created a list of potential star clusters in the Catalog of Open Cluster Data (Kharchenko et al. 2005) suitable for this project using a small number of basic selection criteria (Table 1) chosen to identify systems suitable for multi-object spectroscopy of solar analogs that are close enough to have members sufficiently bright to detect small-amplitude RV variability and old enough to limit stellar jitter. We imposed restrictions on cluster size (R_{cen} in Table 1, the core radius derived by Kharchenko et al. 2005) and richness to ensure good multiplexing efficiency, and placed limits on age and metallicity to exclude clusters with stars that exhibit excessive surface activity (thereby mimicking or masking the Doppler RV variations of a companion) and increase the likelihood of gas giant planet formation. From the list of 124 clusters meeting the first four criteria in Table 1 we identified ~ 30 matching clusters. Ultimately we selected NGC 2516 and NGC 2422 as our targets as they were the richest clusters observable during our first observing run in November 2013. These ~ 140 Myr and ~ 75 Myr old open clusters are within 500 pc, rich in solar analogues, have angular sizes that are well-matched to the multiplexing capabilities of M2FS, and have recent photometric membership catalogs sufficiently deep for selecting solar-analog members (Jeffries et al. 2001; Prisinzano et al. 2003, hereafter J01 and P03).

Individual targets in NGC 2516 were drawn from the sample of stars studied in J01. We selected all stars they identified as photometric single (79) or photometric binary (47) members having colors and magnitudes consistent with F5V–K5V spectral types. This sample of 126 stars was then cross-matched with the UCAC4 catalog (Zacharias et al. 2013) and the UCAC4 coordinates used to prepare the plug plate. In NGC 2422 we selected all objects with colors and magnitudes consistent with F5V–K5V in the membership list of P03. Due to a smaller number of members in

TABLE 1
CLUSTER SELECTION CRITERIA

Criteria	Value	Comment
Dec (deg)	$< +10$	Visible at Magellan
DM	10.0	Bright enough for pRVs
Age (Myr)	$\gtrsim 100$	Limit stellar activity
R_{cen} (deg)	$\lesssim 1.0$	Match to M2FS FOV
Fe/H	$\gtrsim -0.3$	Enhance HJ formation
$N_{\text{F5-K5}}$	$\gtrsim 80$	Match to number of fibers

our field of view, we expanded our selection out in color from the main sequence defined by P03 members using the UCAC4 catalog until we had sufficient targets to fill the available fibers, eventually selecting an additional 25 stars in our adopted pointing in this manner. We then cross-matched the P03 targets with UCAC4 for astrometry. With 128 available fibers, we are able to target every star in each half-degree field that could plausibly be a solar-analog member. Table 2 provides a summary of the clusters, our adopted pointings, and the stellar targets therein.

We selected an additional field (also within NGC 2516) with thirty-two sources with magnitudes (assuming membership) and colors consistent with B8-A4 stars ($B-V = -0.1 - 0.113$; $M_V = 0 - 1.7$). These stars possess essentially featureless spectra – apart from telluric features – in our wavelength range and hence can serve as useful probes to monitor the instrumental point spread function (PSF) over the full field of view of the spectrograph cameras.

Finally, we selected six stars with similar RAs from the GAIA RVS catalog (Soubiran et al. 2013) for use as radial velocity standards. One of these – HIP 48331 – was observed repeatedly and is used as a primary reference to track our RV measurement precision over the duration of the program. Although this star hosts an exoplanetary companion, the induced RV semi-amplitude is only 0.8 m/s (Pepe et al. 2011), far below our measurement precision and so its variability is irrelevant for our purposes. A summary of the standard stars used for this study is presented in Table 3.

2.2. Instrument Configuration

The Michigan/Magellan Fiber System (M2FS) is a multi-object, optical (3700 - 9500 Å), fiber-fed spectrograph that can take simultaneous spectra of up to 256 targets over a half-degree field-of-view at a wide variety of resolutions ($R \sim 500-55,000$). The fibers accept light from the sky at the f/11 Nasmyth E focal surface of the Magellan/Clay 6.5 m telescope at Las Campanas Observatory. Each fiber samples the sky through a 1.2 arcsecond aperture; fibers can be packed to within 14 arcseconds of one another with no restrictions within the M2FS field of view and are held in place by plug plates drilled in advance of an observing run using astrometry for the desired targets.

The fibers terminate at the focal surface of the collimator/cameras belonging to a pair of identical quasi-Littrow spectrographs. For historical reasons, these are identified as the ‘red’ and ‘blue’ M2FS arms, each fed by 128 fibers. The spectrographs are equipped with traditional and echellette gratings for low and medium resolution work as well as an R2.0 echelle grating with a prism cross-disperser for high-resolution use. Filters located just below the fiber termination surface isolate specific orders, necessary for use in echelle and echellette modes. Each arm uses an E2V 4k x 4k anti-fringing CCD with 15 μm pixels. Additional details can be found in Mateo et al. (2012). Figure 1 shows an example frame from our program.

M2FS incorporates a slit mechanism placed just after the ends of the fibers at the spectrograph collimator/camera focal surface; details of this mechanism are provided in Bailey et al. (2012b). For all of the HiRes observations used in this paper, we employed the 45-micron wide slit (the narrowest

TABLE 2
TARGET CLUSTER AND POINTING INFORMATION

Cluster	Messier	RA (2000)	Dec. (2000)	Age (Myr)	Dist. (pc)	E(B-V)	N_{ep}	N_{targ}	V	B-V
NGC 2516	...	7:58:42	-60:46:36	141	346	0.11	12	126	11.68-15.09	0.46-1.26
NGC 2422	M 47	7:36:30	-14:29:42	72	491	0.07	10	125	12.20-16.10	0.45-1.43

NOTE.—The coordinates listed correspond to our field centers and, although near, are not at the cluster center. Both distances and the reddening value for NGC 2422 are from Kharchenko et al. (2005). Target photometry is from J01 (NGC 2516) and P03/UCAC4 (NGC 2422). The reddening value for NGC 2516 is taken from Sung et al. (2002). The age for NGC 2516 is from Meynet et al. (1993) and for NGC 2422 from Loktin et al. (2001). We note that Kharchenko et al. (2005) gives ages of 120 Myr NGC 2516 and 132 Myr for NGC 2422, albeit with errors ~ 70 Myr.

TABLE 3
STANDARD STARS

Target	N	V_{mag}	RV (km/s)	$v \sin(i)$ (km/s)	Sp. Type	T_{eff} (K)	log(g)	[Fe/H]	[α /Fe]
HIP 48331	35	7.67	-9.510 ± 0.005	0.9	K5V	4455 ± 80	4.67	-0.18 ^a	...
HIP 13388	2	8.09	65.606 ± 0.009	2.7	K1V	5095 ± 64	4.59	-0.15	0.02
HIP 10798	5	6.33	7.469 ± 0.007	2.7	G8V	5481 ± 80	4.63	-0.44	0.17
HIP 22278	3	8.52	23.456 ± 0.014	3.6	G5V	5721 ± 65	4.22	0.13	-0.01
HIP 19589	1	8.46	-5.500 ± 0.024	3.6	G0V	5825 ± 90	3.75	-0.17	0.13
HIP 31415	1	7.70	-7.479 ± 0.012	4.5	F6V	6172 ± 60	3.94	-0.31	0.12

^aTaken from Santos et al. (2005) as Casagrande et al. (2011) flags these measurements as of poor quality, though Santos reports an error of 0.19.

NOTE.—This table lists the literature properties and number of epochs we obtained of the standard stars observed for this program. RVs, magnitudes, and spectral types are taken from Soubiran et al. (2013). $v_r \sin(i)$ values are from Głębocki & Gnaniński (2005). Stellar parameters are taken from Casagrande et al. (2011).

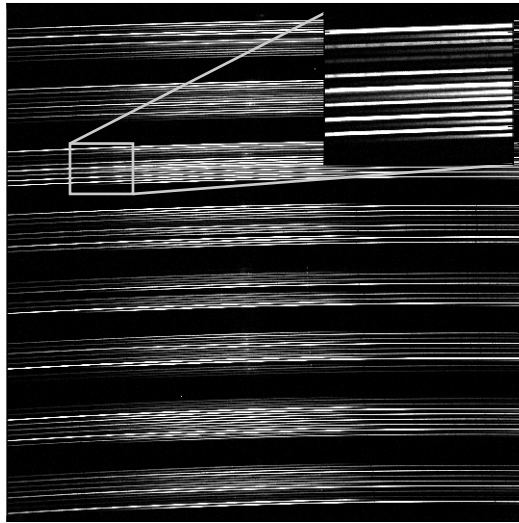


Fig. 1.— An example science frame in NGC 2516. M2FS fibers are bundled in groups of sixteen at the camera focal plane, and although we use every other fiber we also use a two-order passband, resulting in the groups of sixteen spectra. The larger gaps in the image reflect spacing between adjacent bundles of fibers and are used to estimate the scattered light in the image. Each fiber maps to a consecutive pair of apertures (best seen in the inset): the lower is order 50 (unused) and the upper is order 49. The variability in this frame is a function of both target magnitude and fiber throughput.

available) which projects to approximately three pixels at the detectors. For this configuration we found an effective resolution of in 40-60k range for most fibers (c.f Figure 2), subject to focus variations. Because the slits are positioned after the fibers we sacrifice roughly 60% of the incident light.

For this study, we employed a two order filter with a design passband of 7050–7370 Å (M2FS echelle orders 49 and 50): the use of a filter is necessary to prevent spectral orders from one fiber overlapping with those of another and a two order filter limits us to every second M2FS fiber for a multiplexing factor of 128. As few target clusters would offer more than about 100 targets in a single M2FS field this decision does not appreciably affect our multiplexing capability. The passband was selected after careful consideration of the optimal wavelength region to carry out telluric-reference RV measurements of solar analogue stars. We used the formalism of Butler et al. (1996) combined with synthetic spectra from the PHOENIX grid (Husser et al. 2013) to es-

timate the RV uncertainties for slowly-rotating, main-sequence stars with effective temperatures between 4000 and 7000 K for a range of M2FS orders red-ward of about 6800 Å (where telluric features become common). This uncertainty was then added in quadrature with the wavelength reference uncertainty in each order determined by applying the same formalism to the telluric absorption features present in the empirical telluric spectrum from Wallace et al. (2011). Results of this analysis are shown in Figure 3: we show our estimates of attainable velocity precision for Sun-like, slowly rotating stars observed at two fiducial resolving powers and S/N levels for each M2FS order with appreciable telluric lines.

In practice we only obtain useful data from the first portion of order 49 (7160–7290 Å). Our filter was manufactured prior to the discovery of a slight difference in the intended and manufactured echelle grating blaze. This rendered data from order 50 to be of little use, truncated the redder portion of order 49, and limited system throughput by a factor of two (see Figure 4). This limited band-

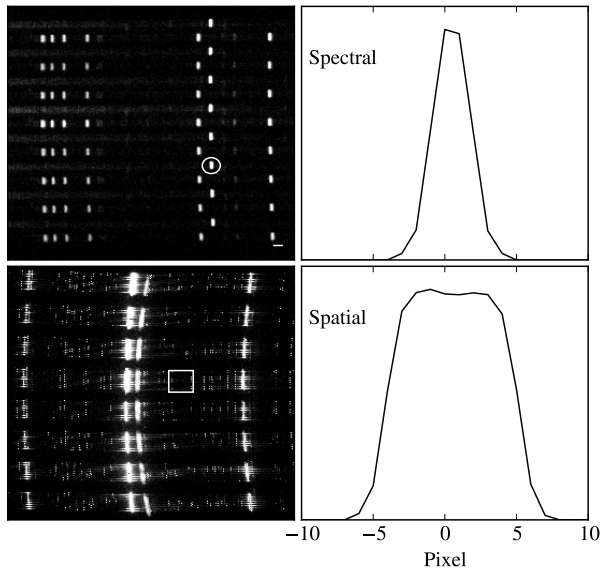


Fig. 2.— This figure shows various aspects of an M2FS ThArNe calibration image (lower-left) made in our configuration. The upper-left panel is detailed view of the boxed region. In it the small horizontal bar to the lower-right of the image is 10 pixels long and the line profiled in the right two panels is encircled. The FWHM of the lamp lines across the images corresponds to ~ 3 pixels on average ($R \sim 50,000$).

pass was still able to deliver excellent RV precision (Section 5.2.1), and manageable S/N for stars in our target clusters. In early 2016 we started verification tests on a new filter designed to cover the 7160–7360 Å region, adding an additional 14 major lines and recovering the lost throughput. We anticipate this will improve our achievable velocity precision by $\sim 15\%$ where we are not limited by systematics and do not anticipate any negative impact on our program.

2.3. Observing Procedure

Since we were looking for radial velocity variations among stars in clusters that might harbor exoplanetary systems, our observing procedure involved repeat observations of our target fields (Table 2) with M2FS. To date, we have observed our pointings in NGC 2516 and NGC 2422 12 and 10 times, respectively. We also obtained 35 observations of our principle RV standard HIP 48331 along with a small number of observations of the other comparison standards (Table 3). The specific dates of the observations will be summarized

in a later paper describing our time-series spectroscopy; for the purposes of the present paper we simply note that the data were obtained during runs in November 2013, February 2014 and December 2014.

As noted earlier, fibers are positioned at the focal surface of the telescope with M2FS using aluminum plug plates that are manually installed and plugged. For a given field, each assigned fiber is positioned at a specific hole in the plate marked for that fiber. We typically deployed 128 fibers for the NGC 2516 and NGC 2422 fields, though with dead or otherwise inactive fibers excluded. Once plugged, a typical observation then consists of acquiring the field using a set of ancillary fibers and imaging optics aligned to reference stars in each field. Typical total exposure times for each observation used in this paper were 2 hrs and 2.5 hrs per visit for NGC 2516 and NGC 2422, respectively. Most visits consisted of 3-5 individual exposures to aid in cosmic-ray removal and to enable measurement of the photon midpoint for barycentric correction. This yielded a median S/N of ~ 55

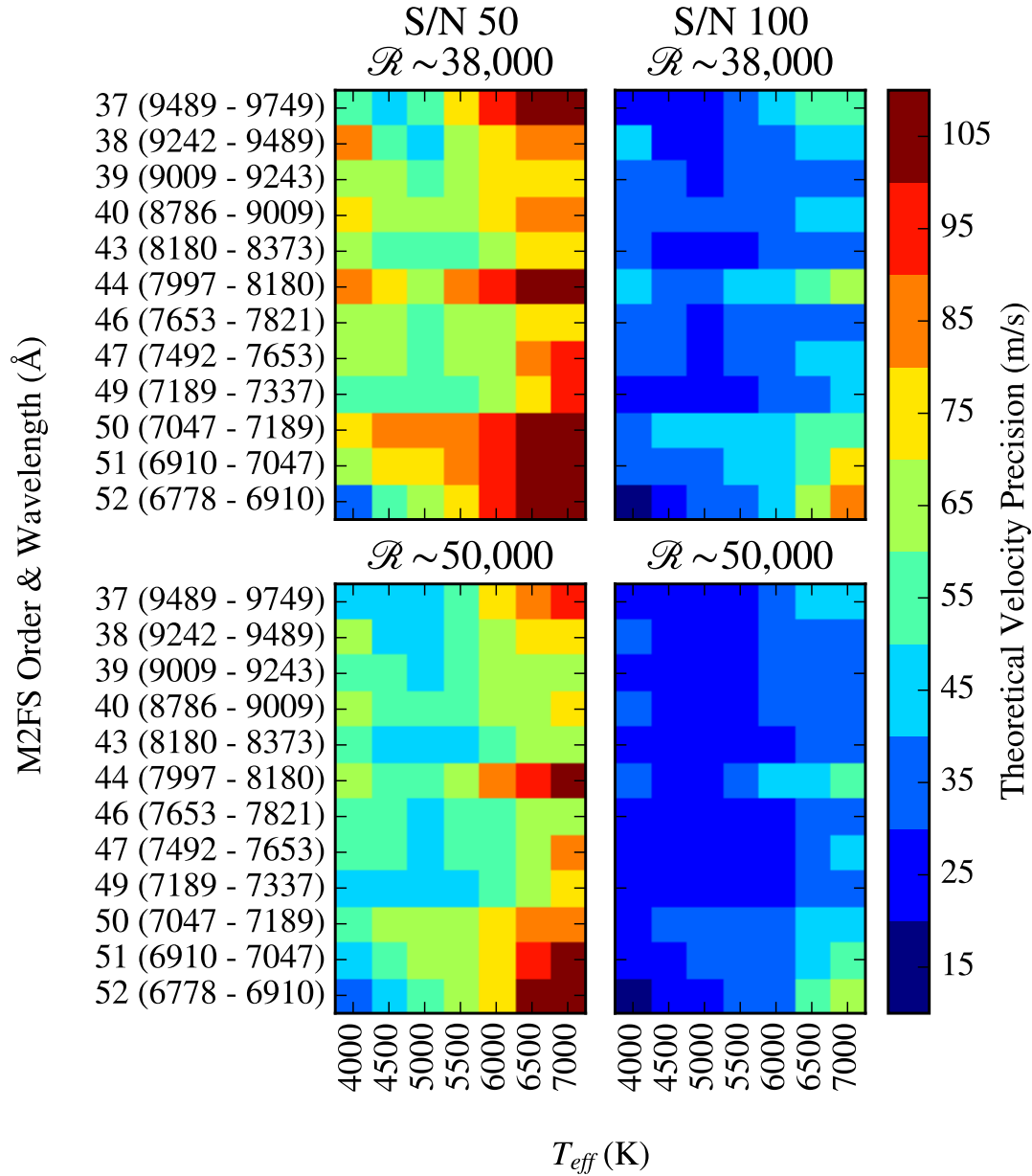


Fig. 3.— The velocity precision attainable for slowly rotating ($v_r \sin(i) = 5$ km/s), Solar abundance, dwarfs stars with T_{eff} between 4000 K and 7000 K when using telluric lines as the wavelength reference, according to the formalism of Butler et al. (1996). Each individual plot gives M2FS echelle order number and nominal wavelength range on the vertical axis and T_{eff} on the horizontal axis. In each case a $\log(g)$ of 4.5 is used, though results are not significantly affected by this choice. The two columns correspond to S/N of 50 and 100 and the rows to $\lambda/d\lambda$ of 38,000 and 50,000. Colors correspond to the attainable RV precision. It is interesting to note that this plot quantifies the assertions of Griffin & Griffin (1973) from some 43 years ago.

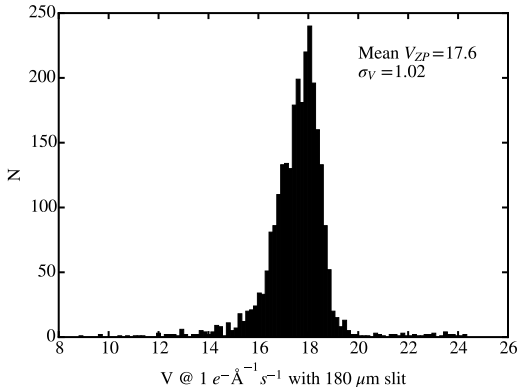


Fig. 4.— A plot of M2FS system throughput as calculated for each of our 2700 spectra. Values have been corrected for both variations in fiber throughput and for the throughput losses imposed by our use of the $45 \mu\text{m}$ slit ($\sim 60\%$) and assume our median seeing of $\sim 0.8''$. For other M2FS instrument modes we find a typical zero point of 18.3 ± 0.3 mag, significantly fainter than measured for these spectra. This loss is a direct result of our filter bandpass edge falling just prior to the blaze peak. This is corrected in the second version of our filter.

($\sim 1\sigma$ range 15 - 70) per 1D extracted pixel (~ 90 per resolution element). A detailed table of our individual observations and the targets therein will be presented in our next paper. For each observation we obtain calibration data consisting of a Thorium-Argon-Neon lamp exposure and a quartz lamp exposure either before or following the science frame. On some nights during which our targets were observed we also obtain either evening or morning twilight spectra.

RV standard observations are performed by placing a single fiber in a standard hole on the fiber plug plate and offsetting from the field center. Remaining fibers are left in their positions and see only sky. Typically three exposures of two minutes each are used to obtain a spectrum of $S/N \sim 240$ per extracted 1D pixel. Finally we obtained four epochs (1 or 2 per observing run) of the telluric standard calibration field in NGC 2516. These spectra have a median S/N of 160 and were obtained in 3 to 5 exposures totaling roughly one half hour.

3. Reduction

3.1. Image Processing

Basic data reduction follows a mostly traditional path using a custom set of Python tools written for M2FS. The quadrant images produced by the CCD's four amplifiers were bias corrected by subtracting the median overscan column and then row. We then converted counts to electrons and used the Python implementation of the L.A. Cosmic algorithm (van Dokkum 2001) to detect cosmic rays: this algorithm takes the Laplacian of the image and identifies cosmic rays using their steep intensity gradient. The quadrants were then packed together and stored with a variance frame consisting of electrons plus the square of each quadrant's read noise and a bad-pixel mask.

We created a cleaned, summed image by adding the electrons and variances of each pixel across a sequence of frames. Masked pixels in each component frame were repaired with their expectation value based on the other frames. A scaling value was computed for each frame to normalize throughput and exposure time variations by using the total time-normalized counts of all spectra as a proxy for throughput variability. Bad pixels in each frame were then repaired using the expect-

tation value determined from the good pixels in other frames and the frame scaling values. The variance of the final, summed pixel was inflated appropriately at every impacted pixel.

Typically one would flat-field the resulting frames, however Quartz trace flats of comparable signal-to-noise take an impractical amount of observing time and M2FS does not presently have a means of obtaining uniformly illuminated CCD frames. Engineering work shows M2FS CCDs are free from large defects and indicate pixel-to-pixel sensitivity variations of about 1.7% and only 0.25% of pixels are significantly hot or cold.

We subtracted a combined dark current and scattered light map, an example of which is shown in Figure 5 along with the image prior to and post subtraction. This map was computed by first modeling and removing the amplifier glow in each corner by fitting a 2D Gaussian surface. All remaining pixels within about a standard deviation of the mean light level in the dark regions between bundles of 16 fibers were then selected as “scattered light” pixels and used to fit polynomials across the image. The resulting map was Gaussian smoothed using a 32 x 64 pixel rectangle ($\sim 1.5 \times 3$ fiber spacings) and subtracted from the image. Without this step, these components would amount to about 150 e^- per 1D pixel in our extracted spectra, ranging from $\sim 5 - 50\%$ of our extracted signal for our brightest to faintest targets.

3.2. Extraction

Each processed frame was then extracted using the PyRAF task `apall`. We first identified the approximate aperture locations and traces using dome flats taken during the day with all usable fibers plugged. The apertures were then median shifted to the locations of the quartz traces taken with each exposure to account for any temperature drift or repositioning errors in the instrument. We then extracted both the science and variance frames without variance weighting using identical apertures. Finally we continuum normalized the spectra by iteratively fitting a polynomial, each time excluding points 1 sigma below or 2 sigma above. An example of order 49 for a \sim F5V, G5V, & K5V star in our sample is shown in Figure 6. We do not wavelength calibrate our spectra in a traditional sense as wavelengths are determined as

part of the modeling process.

4. Analysis

We measured each target’s stellar properties (e.g. T_{eff} , $[\text{Fe}/\text{H}]$, $[\alpha/\text{Fe}]$, $v_r \sin(i)$) and line-of-sight radial velocity (RV) by fitting a model of each extracted, normalized spectrum to the spectrum in 1D pixel space. This approach is similar to the popular gas cell approach where molecular absorption lines from a well-calibrated gas cell (e.g. I_2 , Ammonia) are used as a simultaneous probe of pixel wavelengths and the instrumental point-spread function (PSF). Here we make use of the abundant atmospheric H_2O lines in the 7230 Å region as the imprint of a giant gas “cell.” A variant of this idea was originally proposed by Griffin & Griffin (1973) more than 40 years ago and has been used with success to measure RVs in both the optical (Cochran 1988; Figueira et al. 2010) and the infrared (Blake et al. 2007; Prato et al. 2008; Seifahrt et al. 2010; Blake et al. 2010; Crockett et al. 2011; Bailey et al. 2012). These studies have demonstrated that telluric features are stable to 10 m/s. This should not come as a surprise as all of the water and the general bulk of our atmosphere is within the first 8 - 16 km where typical bulk motions are below 10 m/s and not along the line-of-sight. We will quantify this source of uncertainty when we discuss our achieved RV precision in Section 5.2.1.

The model is constructed by combining a template of the telluric absorption spectrum, $T(\lambda)$, one or more synthetic stellar spectra, $S(\lambda; T_{eff}, [\text{Fe}/\text{H}], [\alpha/\text{Fe}], v_r \sin(i), \text{RV})$, a synthetic sky emission spectrum, $Sky(\lambda)$, and a Solar spectrum $Sun(\lambda; RV_\odot)$.

$$M(\lambda) = T(\lambda)^\alpha \cdot (S(\lambda; T_{eff}, [\text{Fe}/\text{H}], [\alpha/\text{Fe}], v_r \sin(i), \text{RV})^\beta + \gamma \cdot Sun(\lambda + s; RV_\odot)) + \eta \cdot Sky(\lambda) \quad (1)$$

This model is then resampled onto pixels, convolved with a model of the 1D projection of the PSF, and normalized.

$$M(\text{pixel}) = \frac{PSF(\text{pixel}; \boldsymbol{\sigma}) * M(\text{pixel})}{N(\text{pixel}; \boldsymbol{\zeta})} \quad (2)$$

In the above equations the scalars α , β , γ , η , s , and vectors $\boldsymbol{\sigma}$ and $\boldsymbol{\zeta}$ are model parameters which

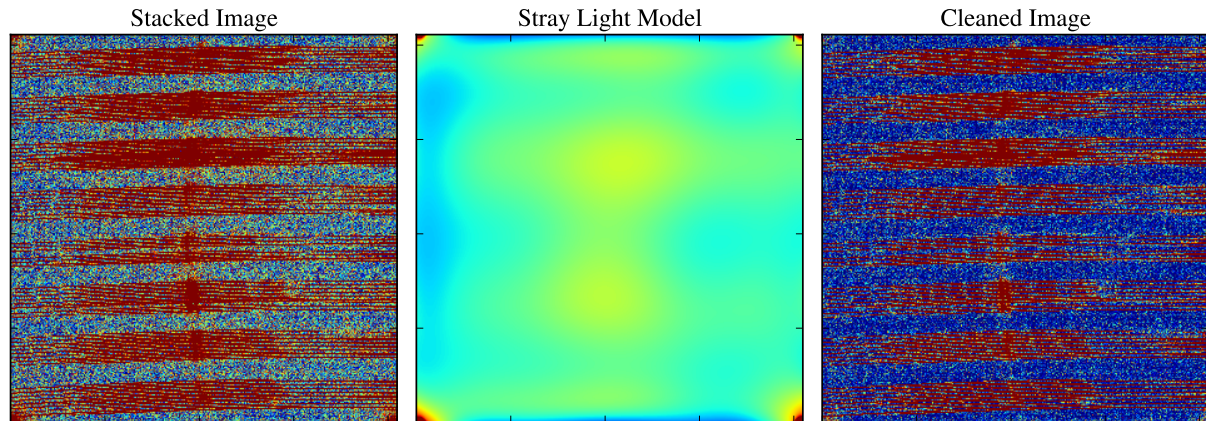


Fig. 5.— Left to right: A stacked science frame, a map of scattered light and dark current, and the cleaned frame. Amplifier glow and spectra are heavily clipped in the frames. The central, bright, vertical swath stems from Littrow ghosts. All three images share the same color scale.

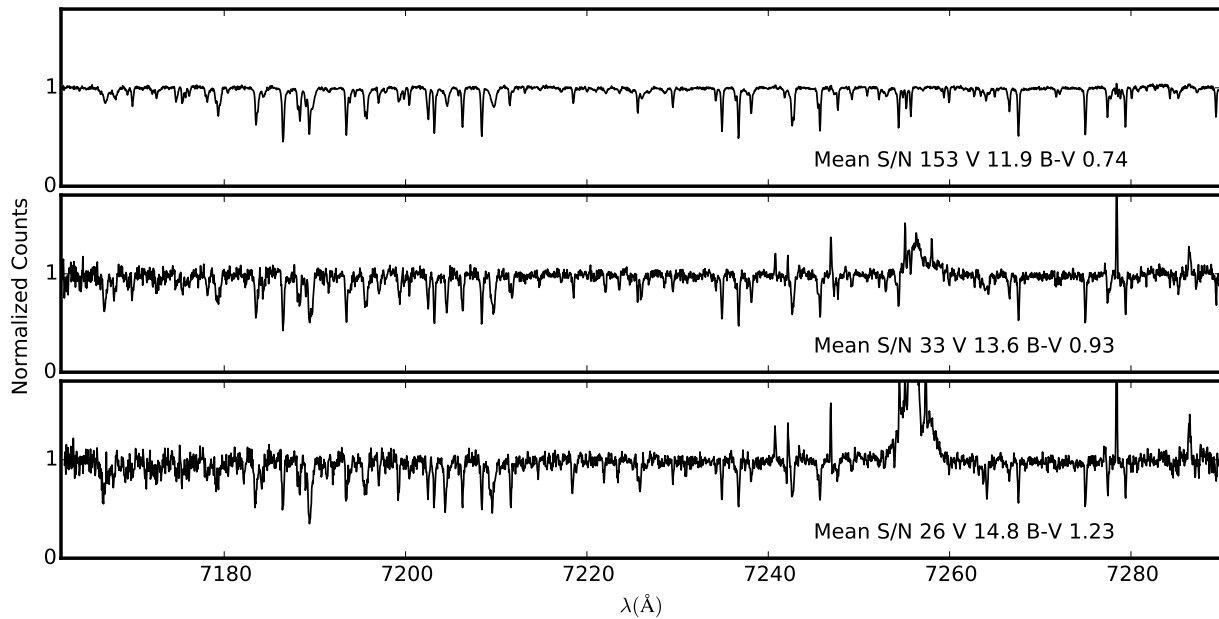


Fig. 6.— Spectra of representative F5, G5, and K5 target spectra. Note that sky emission lines become increasingly prominent for fainter targets. The large defect at $\sim 7255 \text{ \AA}$ is M2FS's Littrow ghost.

TABLE 4
MODEL PARAMETERS

Component	Symbol	Number	Comments
Wavelength	μ	≤ 8	$\lambda(pixel) = \sum_i^8 \mu_i L_i(pixel)$
PSF	σ	1	The PSF FWHM
		3	$FWHM(pixel) = \sum_i^2 \sigma_i L_i(pixel)$
		5	A 5th order Hermite parameterization
		22	Butler et al. (1996) parameterization
Nomalization	ζ	12	$norm(pixel) = \sum_i^{11} \zeta_i L_i(pixel)$
Stellar Temperature	T_{eff}	1	Snaps to 100 K grid ^a
Iron Abundance	[Fe/H]	1	Snaps to 0.1 dex grid
Alpha Abundance	[α /Fe]	1	Snaps to 0.1 dex grid
Stellar Rotation	$v_r \sin(i)$	1	
Radial Velocity	RV	1	
Airmass	α	1	Scale atmospheric transmission
Veiling	β	1	Scales stellar absorption lines in unison.
			Held at unity when fitting stellar parameters
Solar Flux	γ	1	Fractional contribution of solar flux
Solar RV	RV_{\odot}	1	
Solar Offset	s	1	Offset between PHOENIX and Kurucz wavelengths
Sky Emission	η	1	Scale SkyCalc spectrum

^aTemplate spectrum with nearest value is used.

will be described in the next section and are summarized in Table 4.

4.1. Model Input

4.1.1. Stellar Light

Our pipeline uses the PHOENIX grid as it samples a large stellar parameter space (far beyond our region of immediate interest), is the successor to the grid used in Bailey et al. (2012), and in no small part because it is the grid for which we attained the best RV precision for our RV standard. To verify this point we also checked both the Coelho (2014) grid and the AMBRE grid (de Laverny et al. 2012) and found both to result in larger RV measurement errors for our RV standard. Prior to modeling we up-sampled the PHOENIX grid (see Table 5) in the parameter space relevant to our target stars using linear interpolation by way of the SciPy function `map_coordinates`. Library spectra are normed by the maximum continuum value in the fitting region and linearly interpolated onto a constant $d \log(\lambda)$ grid, adopting the largest step size present in the raw spectrum, just prior to use in the modeling pipeline.

During fitting, the surface gravity is tied to the effective temperature via Eqn. 7 which is derived from the mass-luminosity, temperature-luminosity, and mass-radius relations for lower main-sequence stars as our fits do not appear to be particularly sensitive to variations in $\log(g)$ among our main sequence targets. This weak dependence is seen in other techniques as well: Casagrande et al. (2011) reports that even variations as large as a half-dex affect T_{eff} by only a few tens of Kelvin. We calibrated the relation using Solar values corrected for age per the plot in Ribas (2010), $L = 0.85L_{\odot}$, $R = 0.925R_{\odot}$.

$$R \propto M^{0.9} \quad (3)$$

$$L = L_{\odot} \left(\frac{M}{M_{\odot}} \right)^4 \quad (4)$$

$$L = 4\pi R^2 \sigma T_{eff}^4 \quad (5)$$

$$g = \left(\frac{L_{\odot}}{4\pi\sigma} \right)^{4/11} \frac{GM_{\odot}}{R_{\odot}^{30/11} T_{eff}^{16/11}} \quad (6)$$

$$\log(g) = \log\left(\frac{9.44 \times 10^9}{T_{eff}^{16/11}} \right) \quad (7)$$

This input brings with it the astrophysical parameters T_{eff} , $[\text{Fe}/\text{H}]$, $[\alpha/\text{Fe}]$, $v_r \sin(i)$, and RV along with a feature depth parameter β which allows fudging the optical depths of all the stellar lines in unison (we note that this is a simplification as lines are not expected to scale in unison). In the event of a spectroscopic binary we can enable multi-component modeling, using two sets of these parameters and an additional multiplicative parameter for the ratio of flux received from the two stars.

4.1.2. Telluric Transmission

We considered two options for the telluric transmission model: the NSO empiric transmission spectrum (Wallace et al. 2011) and the synthetic TAPAS model (Bertaux et al. 2014), nominally tailor made for the atmospheric conditions during each observation. The NSO spectrum derives from data obtained on the McMath-Pierce solar telescope using the Fourier transform spectrograph (FTS) in the late 1980s. TAPAS spectra are computed as described in Bertaux et al. (2014) for the conditions of each exposure.

When using TAPAS spectra in constructing our models for HIP 48331 we measured an RV 286 ± 8 m/s larger than when using the NSO spectrum as the template and also observed a reduction in RV precision (c.f. Section 5.2.1). This shift is on the order of the uncertainty of the O_2 and H_2O line positions in the HiTran database (Rothman et al. 2009) and so is perhaps not unexpected given that it is used as the data source for TAPAS. It is interesting to note that this is also of order the shift caused by mixing Edlén (1966) and Ciddor (1996) air/vacuum relations (e.g. converting one way with Ciddor and back with Edlén), however we are unable to ascertain a list of conversions applied between the original data and the output TAPAS spectrum and are unable to offer any firm conclusions regarding the source of the shift. We do measure better χ^2 values when using TAPAS spectra and suggest that the TAPAS pipeline models differences in atmospheric line strengths between Kitt Peak and Las Campanas well. Given the reduced RV precision we used the NSO FTS data for our analysis. This input brings with it the parameter α to logarithmically scale the absorption features as a proxy for airmass.

TABLE 5
SYNTHETIC GRID SPACING

Grid	$\Delta T_{eff}(K)$	$\Delta \log(g)(dex)$	$\Delta [Fe/H](dex)$	$\Delta [\alpha/Fe](dex)$
PHOENIX	100	0.5	0.5	0.2
Resampled PHOENIX	100	0.1	0.1	0.1

4.1.3. Sky Emission

We used the ESO SkyCalc tool (Noll et al. 2012; Jones et al. 2013) to obtain night sky emission spectra for our wavelength region. These spectra match the locations of the night sky emission lines well, though they do not always perfectly match their relative strengths. This input adds a multiplicative scaling parameter, η , to adjust the predicted count rate.

4.1.4. Instrumental Effects

The modeling code also includes inputs for the instrumental dispersion relation, point spread function (PSF), and allows for inaccuracies in our continuum normalization. The dispersion relation is a set of Legendre polynomial coefficients (μ) which yield the wavelengths at each extracted pixel. We used a second set of Legendre polynomial coefficients (ζ) to compute a normalization polynomial that accommodates errors in continuum normalization during extraction.

The PSF is widely understood (c.f. e.g. Butler et al. 1996; Bean et al. 2010; Bailey et al. 2012) to have a significant impact on the precision with which line centroids can be recovered and ultimately the RV precision. We investigated this effect by modeling our PSF with a Gaussian, a Gaussian with width quadratically varying along the order, the multi-Gaussian parameterization of Butler et al. (1996), and a 5th order Gauss-Hermite series (Gao et al. 2015) and then determining which prescription minimized the RV standard deviation for our RV standard.

4.2. Modeling Process

4.2.1. Model Construction

To compute the model described in Equations 1 and 2 the code will first fetch the synthetic spec-

trum of nearest temperature, surface gravity, iron, and α -element abundance from our grid (recall $\log(g)$ is computed per Eqn. 7) along with the telluric absorption, Solar, and pointing dependent emission spectra. These spectra are all in excess of $R \sim 600,000$.

The telluric transmission spectrum is scaled logarithmically by α and the sky emission and Solar spectra are scaled multiplicatively by η and γ , respectively. The solar spectrum is Doppler shifted by multiplying the wavelength grid by the appropriate Doppler factor.

The stellar spectrum is normalized by the maximum flux in the wavelength region to perform a simple continuum normalization while preserving the slight blackbody effect in our narrow region. In the case of a multi-star fit normalization of each spectrum is still carried out in this manner. The spectrum is scaled logarithmically by β to account for any mean discrepancy in line depth and is then rotationally broadened via convolution with a kernel computed based on Equation 17.12 in Gray (1992)¹. Finally the spectrum is Doppler shifted by multiplying the wavelength grid by the Doppler factor.

When computing a binary model this process is repeated for each star and a weighted average of the two spectra is taken after they are placed on the sub pixel grid in the following step. In this situation the weight is an additional free parameter (constrained between 0 and 1). We investigated combining the stellar components in a manner that enforces their relative flux from the synthetic library however this often led to grossly inappropriate minima. When modeling a telluric standard spectrum we model the stellar compo-

¹We do not use the `lsf_rotate` library function from Hubeny & Lanz (2011) as there are numerical and functional errors in the construction of the kernel that cause discontinuities in χ^2 as a function of $v_r \sin(i)$.

ment as unity.

If including scattered Solar light the solar spectrum is multiplicatively scaled by γ , s is added to the Solar wavelength grid, and then the grid is multiplied by the appropriate Doppler factor.

Each of the components is linearly interpolated onto a 10^{th} pixel wavelength grid computed from the dispersion relation. We note that cubic spline interpolation significantly decreased our RV stability. These component spectra are then combined as in Eqn. 1.

This model is then convolved with the PSF kernel representing the instrument’s point spread function as mangled by our simplistic extraction. The kernel size was selected such that the kernel is less than 10^{-4} at the window edge and the kernel is always constrained to be positive. To maintain a modicum of speed pixel dependent convolutions are carried out via a FORTRAN subprogram. When using an asymmetric PSF we noted that the center of the enclosed power was not generally located at the central sub-pixel nor at some constant offset. We observed a shift for typical, good fits of 1.5 ± 0.86 pixels redward with the Hermite parameterization. Constraining the centroid to ± 0.05 pixels of the center confers substantial improvements to RV precision (See Section 5.2.1). In the limit of a linear dispersion relation this effect would correspond to a simple pixel shift and would not be expected to have any impact on results, however our wavelength solutions are not linear. Our code constrains the centroid by shifting the PSF kernel and hence constrain the center of enclosed power to within ~ 100 m/s of the central sub-pixel. Interpolated shifts or a PSF parameterization which constrains the enclosed power may be worth future investigation.

After convolution, the sub-pixel values are averaged to yield pixel values and the model is divided by the normalization polynomial, yielding a model spectrum.

4.2.2. Merit Function

To determine the optimal model, we used the χ^2 as a merit function. The fitter computes the weighted mean square error of our model with the normalized spectrum, masking pixels based on a wavelength mask (e.g. for sky lines, if desired), an RV dependent wavelength mask for stellar lines,

and a pixel mask for detector defects and the Littrow ghosts. Wavelength masks are additive: for stability, once masked, a change to the wavelength solution will not cause a pixel to unmask. The weights are computed as the ratio of the square of the continuum normalization to the variance spectrum. We noted a significant upward trend in our best-fit χ^2 with increasing signal (c.f. Figure 7), which we attribute to an improved ability to identify finer errors in our computed model. Visual inspection shows that PHOENIX spectra consistently mismatch stellar line depths and with increasing S/N these mismatches become increasingly significant.

4.2.3. Model Fitting

Prior to fitting we visually reviewed all ~ 2700 spectra and excluded spectra with average continuum S/N less than 12 (per pixel). We limited all our fits to the extent of order 49 with continuum S/N greater than 12 or the columns between pixels 25 and 2700 ($\sim 7160 - 7290$ Å). These column extents were selected such that we have a slight margin at either end with which to estimate the continuum level at the order edges beyond the fitting extent. Generally fits were to all 2675 pixels in this region. We masked pixels affected by extraction artifacts, continuum normalization errors, uncorrected cosmic rays, or Littrow ghosts. After fitting we inspected the results for any failures (generally due to a poor initial RV guess) and either corrected them, flagged them to handle as exceptional cases, or excluded them from analysis.

We optimized the model in stages. 1) For a subset of spectra we first obtained an initial guess for the wavelength solution by eye. These guesses were used to bootstrap initial relations for the wavelength solution in one frame of each arm on each run. The initial PSF width was chosen such that it coincides with M2FS’s nominal resolving power in our configuration without asymmetry and an initial spectral type was chosen assuming Solar abundance and using the (B-V)- T_{eff} relation of Casagrande et al. (2010) with reddening corrected values for B-V. These parameters were then used as the initial values for a round of fits from which we constructed a predictive model of the dispersion parameters as function of M2FS arm, CCD trace position, and night. We found the $4^{th} - 7^{th}$ order wavelength parameters are neither a

function of instrument temperature, (mis)focus, or run and thus adopted a simple polynomial model as a function of aperture position based on the best fit values for all ~ 2600 usable spectra. We only adopt the mean values as an initial guess for the $1^{st} - 3^{rd}$ order parameters and note that the wavelength zero point parameter is predicted for each exposure separately. 2) We then refit all our spectra with the initial wavelength parameters determined in phase one, holding the $4^{th} - 7^{th}$ order wavelength parameters fixed, and adopted the inverse variance weighted means of the best-fit spectral type parameters and $v_r \sin(i)$ values for each star. 3) We performed a final round of fits still holding higher order wavelength parameters fixed, now along with the spectral type parameters and $v_r \sin(i)$. We used the RVs from this final fit as the values we adopt for each star. Except in the case of large amplitude binaries the RV was always started from the adopted multi-epoch mean.

Section 5 describes the precision with which we recover these values. As our initial wavelength guesses are crude we investigated the impact priming our wavelength solution parameters with ThAr calibration fits to verify we were not introducing a fitting bias. For this test we refit all of the RV standard spectra using the IRAF identify task solutions to corresponding ThAr data for the initial wavelength solution. We found no impact. Holding the higher order wavelength parameters fixed improves RV precision by approximately ~ 5 m/s at all signal-to-noise levels (c.f. Sec. 5.2.1). An example fit is shown in Figure 8.

Optimization was carried out using the MPFIT (Markwardt 2009) package to minimize the weighted errors for each unmasked pixel. In previous iterations of our software we used the AMOEBA minimizer: the downhill-simplex optimizer (Nelder & Mead 1965) appears more tolerant of poor initial guesses, but minimization takes a greater number of function evaluations, does not yield a parameter covariance matrix, and requires parameter limits be hacked on as they are not inherent to the algorithm. We also investigated using the MCMC core of Eastman et al. (2013), and briefly explored a genetic fitter, the latter of which proved to be of similar quality but highly inefficient. We found these various methods of optimization to all be of comparable end result but with significantly prolonged computation time.

5. Results and Performance

5.1. Stellar Properties

We estimated the statistical uncertainty of our stellar parameters from the distribution of best fit values relative to their multi-epoch means. We used the results from the second stage of our fitting pipeline (where stellar properties are allowed to vary from epoch to epoch, c.f. Sec. 4.2.3), exclusive of spectroscopic binaries, to obtain fits to 2283 spectra of 214 targets (see Table 6) with which we computed the differences between the single epoch values and the adopted multi-epoch values of the stellar parameter. We then performed kernel density estimation on each parameter and computed confidence intervals. The resulting PDFs are shown in Figures 9, 10, 11, and 12 and the 1σ confidence intervals given in Table 7. In addition to the overall PDFs, the plots give PDFs for subsamples grouped by spectral type and rotation rate ($v_r \sin(i) > 8$ km/s). The selection of 8 km/s as a grouping is largely arbitrary, though corresponds with the point where $v_r \sin(i)$ becomes the dominate source of line broadening relative to the instrumental PSF. Though we do not explicitly show PDFs for groupings in S/N, the PDFs for spectral type show this by proxy; later spectral types are fainter and have lower S/N spectra. We saw no evidence that the PSF form (e.g. Gaussian vs. Hermite series) affected the measured values or their uncertainties.

We estimated the accuracy of our technique for determining T_{eff} , $[\text{Fe}/\text{H}]$, and $[\alpha/\text{Fe}]$ by comparing the values we measured with those in the literature. Tables 8 gives our values for the six standard stars along with those from the literature. Tables 9 then reports the differences in these values: we adopt the averages therein as an estimate of our systematic uncertainties. As an additional check we fitted ~ 900 twilight spectra and report the values and differences thereby obtained. Though these values are of comparable quality, we excluded them from our average as the large number of spectra would heavily bias the results. We tested our $v_r \sin(i)$ accuracy by comparing our values with those reported in Terndrup et al. (2002), with which we have thirty-seven targets in NGC 2516 in common². Our values agree to within 5 km/s for all but four stars, which are all spectroscopic binaries. For the remaining 33

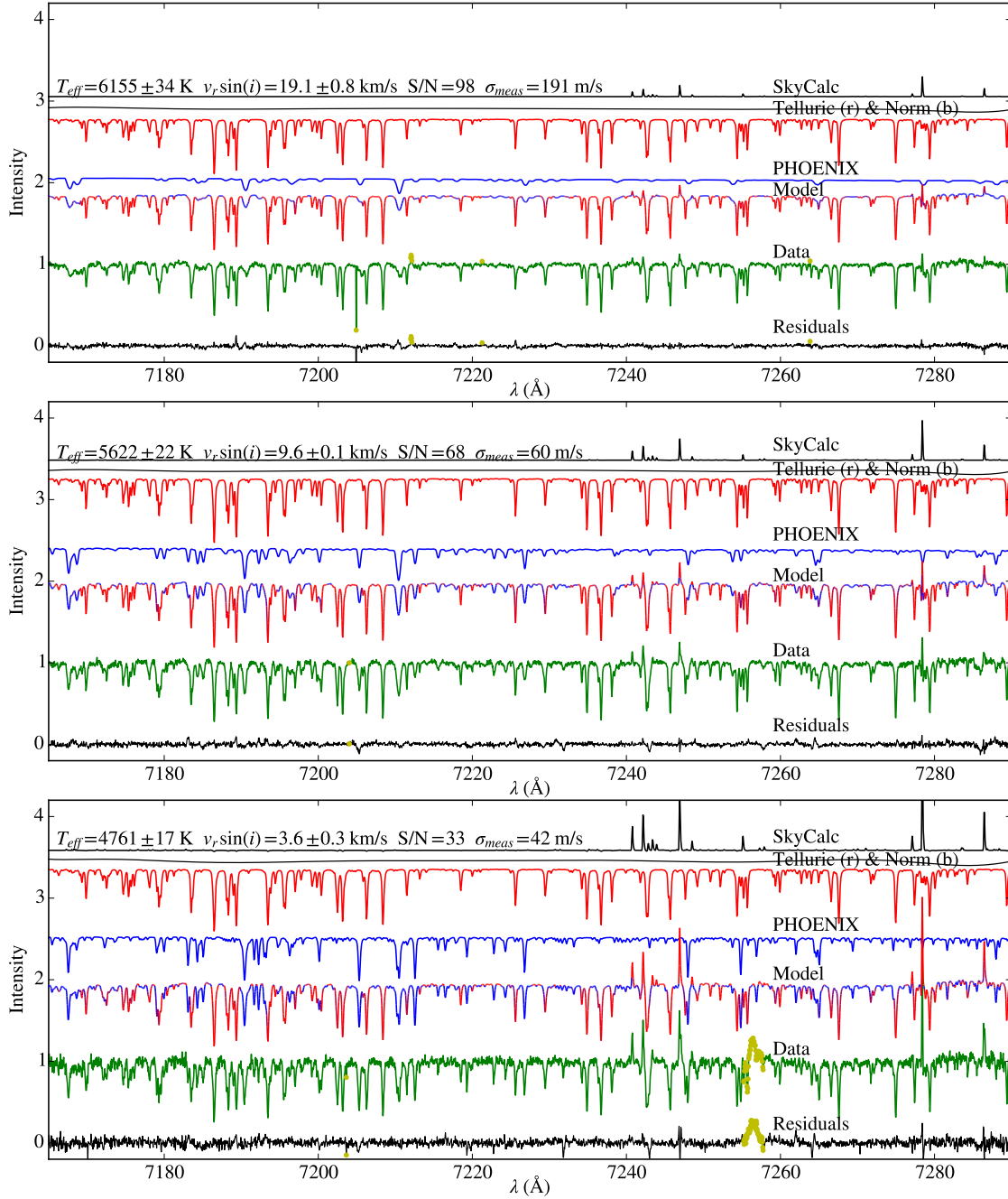


Fig. 8.— Examples of fits to F (top), G (middle), and K (bottom) stars in our sample. Each spectrum is labeled with the adopted T_{eff} , and $v_r \sin(i)$ for the star along with mean S/N and σ_{meas} for the plotted spectrum. From top to bottom in a single plot we show the sky emission component (black), the normalization curve (black), the FTS telluric transmission profile (red), The PHOENIX model (blue), our resulting model of the data (blue and red), the extracted spectrum (green), and the residuals (black). Data and residuals that are masked have yellow points overlaid.

stars our adopted, multi-epoch mean values agree with a standard deviation of 2.2 km/s. We recovered the correct $v_r \sin(i)$ to better than 0.1 km/s in fits to our twilight spectra. Our code is not able to reliably measure $v_r \sin(i)$ values below ~ 2 km/s (roughly one third of our velocity resolution).

Based on this analysis, we report our fits yield typical single-epoch precisions of 75 K, 0.05 dex, and 0.75 km/s for T_{eff} , [Fe/H] and $[\alpha/Fe]$, and $v_r \sin(i)$. We find this translates to mean multi-epoch precisions of ± 30 K, ± 0.02 dex for both [Fe/H] and $[\alpha/Fe]$, and ± 0.3 km/s for $v_r \sin(i)$. Our T_{eff} values are typically cooler than available literature data for our standards by ~ 25 K and we find a similar offset when fitting twilight spectra. Iron abundance values appear elevated by a tenth dex but are driven entirely by HIP 48331: excluding HIP 48331 $\Delta[Fe/H]$ becomes -0.03 ± 0.03 dex, consistent with our twilight fits. We do not see any evidence of a systematic offset in $[\alpha/Fe]$ or $v_r \sin(i)$.

5.2. RV Precision and Accuracy

5.2.1. Precision

Radial velocity variations of stars without a companion stem from one of five sources: (1) an inherent photon noise error (σ_{phot}) arising from the S/N and the number and shape of the stellar and telluric lines, (2) an instrumental error (σ_{inst}) based on the characteristics of M2FS spectra, (3) an error contribution due to our analysis (σ_{anal}), (4) intrinsic stellar variability (σ_{stel}) caused by stellar activity (e.g. stellar flares or star spots), and (5) variability in the bulk atmospheric motion along the line of sight that introduces a Doppler shift on our wavelength reference (σ_{atm}). We assume that all five sources add in quadrature to produce the observed dispersion (σ_{obs}), as follows:

$$\sigma_{obs}^2 = \sigma_{phot}^2 + \sigma_{inst}^2 + \sigma_{anal}^2 + \sigma_{stel}^2 + \sigma_{atm}^2.$$

Under this assumption, the observed velocity dispersion of a star with a known σ_{stel} and observed under conditions with a known σ_{atm} can be used to estimate the quadrature sum of the first three error terms, which we refer to as an effective mea-

²We do not perform this exercise on T_{eff} as the values reported are from colors.

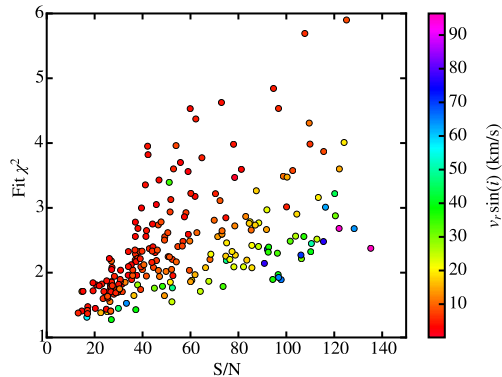


Fig. 7.— This figure shows the average best-fit reduced χ^2 for each of our cluster stars plotted as a function of S/N. Colors denote the rotational velocity measured for each star. There is a distinct upward trend in χ^2 with S/N.

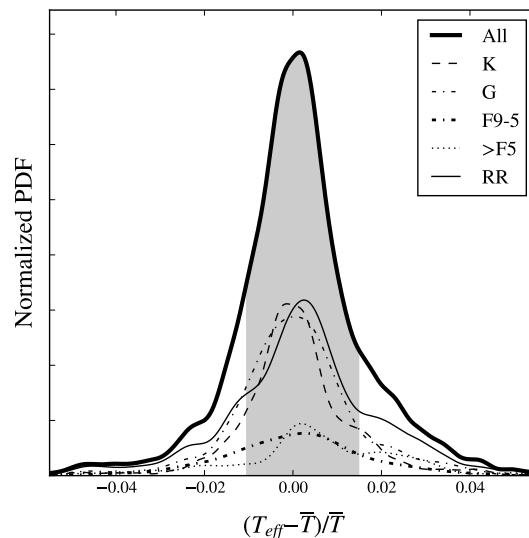


Fig. 9.— This plot shows normalized PDFs for fractional ΔT_{eff} for the entire sample and subsamples of stars as a function of spectral type and stars with $v_r \sin(i) > 8$ km/s (RR). The shaded region corresponds to 1σ for the entire sample.

TABLE 6
PRECISION TARGETS

Cluster	V	B-V	Used	Excluded
NGC 2516	11.68 – 15.09	0.46 – 1.17	108	18
NGC 2422	12.19 – 16.05	0.45 – 1.31	106	19
Total	11.68 – 16.05	0.45 – 1.31	214	37

NOTE.—This table gives the ranges in magnitudes, colors, and number of cluster stars used to determine our statistical uncertainties in T_{eff} , $[Fe/H]$, $[\alpha/Fe]$, and $v_r \sin(i)$. We exclude spectroscopic binaries in this analysis.

TABLE 7
SINGLE EPOCH PROPERTY PRECISION

Property	K5-G7		G7-G2		G1-F5		F4 and hotter	
	Lower	Upper	Lower	Upper	Lower	Upper	Lower	Upper
T_{eff} (K)	–44	+59	–62	+74	–95	+121	–82	+163
$[Fe/H]$ (dex)	–0.06	+0.05	–0.05	+0.06	–0.07	+0.06	–0.07	+0.05
$[\alpha/Fe]$ (dex)	–0.04	+0.04	–0.05	+0.04	–0.07	+0.04	–0.07	+0.04
$v_r \sin(i)$ (km/s)	–0.5	+0.5	–0.3	+0.4	–0.5	+0.7	–1.0	+0.9
Mean S/N	30		60		80		100	

NOTE.—This table gives the upper and lower limits enclosing the central 66% confidence interval for T_{eff} , $[Fe/H]$, $[\alpha/Fe]$, and $v_r \sin(i)$. That is, given measurement of a single epoch, there is a 66% chance we would measure a value within the stated limits for a second epoch. Below each pair of columns we list the mean S/N of stars in each group.

TABLE 8
MEASURED STANDARD STAR PROPERTIES

Ref	T_{eff} (K)	$\log(g)$	[Fe/H] (dex)	$[\alpha/Fe]$ (dex)
HIP 48331 N=35 K5V				
This work	4463 ± 4	(4.7)	-0.05 ± 0.002	0.19 ± 0.006
S05	4505 ± 176	4.71 ± 0.96	-0.18 ± 0.19	...
S08	4715 ± 102	4.39 ± 0.28	-0.32 ± 0.03	...
N09	S08 ^a	S08	S08	0.20 ± 0.18
C11	4455 ± 80	4.67
A12	S08	S08	S08	0.22 ± 0.08
T13	4400 ± 45	4.36 ± 0.1	-0.26 ± 0.14	...
HIP 13388 N=2 K1V				
This work	4991 ± 52	(4.6)	-0.38 ± 0.055	0.26 ± 0.037
C11	5095 ± 64	4.59	-0.15 ± 0.1	0.02
S08	5040 ± 48	4.39 ± 0.08	-0.45 ± 0.04	...
N09	S08	S08	S08	0.22 ± 0.1
HIP 10798 N=5 G8V				
This work	5312 ± 19	(4.6)	-0.54 ± 0.0081	0.14 ± 0.008
V05	5374 ± 44	4.69 ± 0.06	-0.47 ± 0.03	...
C11	5481 ± 80	4.63	-0.44 ± 0.1	0.17
HIP 22278 N=1 G5V				
This work	5652 ± 68	(4.5)	0.04 ± 0.056	0.08 ± 0.046
C11	5721 ± 65	4.22	0.13 ± 0.1	-0.01
HIP 19589 N=1 G0V				
This work	5966 ± 108	(4.5)	-0.30 ± 0.067	0.15 ± 0.057
C11	5825 ± 90	3.75	-0.17 ± 0.1	0.13
K13	5705 ± 79	3.40 ± 0.15	-0.52 ± 0.1	0.28 ± 0.15
HIP 31415 N=1 F6V				
This work	6295 ± 108	(4.4)	-0.55 ± 0.067	0.21 ± 0.057
C11	6172 ± 60	3.94	-0.31 ± 0.1	0.12
Sol N=909 G2V				
This work	5726 ± 2	(4.5)	-0.03 ± 0.00	0.01 ± 0.00

^aValue reported is from S08

References. — (K13 Kordopatis et al. 2013; C11 Casagrande et al. 2011; N09 Neves et al. 2009; S08 Sousa et al. 2008; S05 Santos et al. 2005; V05 Valenti & Fischer 2005; T13 Tsantaki et al. 2013; A12 Adibekyan et al. 2012)

NOTE.— $[\alpha/Fe]$ values for N09 and A13 are the average of Mg, Ca, Si, and (Ti I + Ti II)/2. Note that $[\alpha/Fe]$ values from C11 are not direct measurements and a measured by proxy from a statistical relation reported therein. Solar values are based on fits to ~ 900 twilight spectra. Errors quoted for our stars are based on Table 7. Our $\log(g)$ values are those used during fitting and should not be interpreted as a measurement. The values reported in this table do not include any adjustments for possible systematic errors.

TABLE 9
PARAMETER DIFFERENCES

Target	Type	ΔT_{eff} (K)	$\Delta[\text{Fe}/\text{H}]$ (dex)	$\Delta[\alpha/\text{Fe}]$ (dex)
HIP 48331	K5V	9 ± 37	$+0.26 \pm 0.03$	-0.03 ± 0.07
HIP 13388	K1V	-69 ± 53	$+0.03 \pm 0.05$	$+0.08 \pm 0.09$
HIP 10798	G8V	-87 ± 49	-0.07 ± 0.04	$+0.03 \pm 0.2$
HIP 22278	G5V	-69 ± 94	$+0.17 \pm 0.11$	$+0.09 \pm 0.20$
HIP 19589	G0V	209 ± 124	$+0.05 \pm 0.10$	-0.08 ± 0.13
HIP 31415	F6V	123 ± 124	-0.24 ± 0.12	$+0.09 \pm 0.21$
Average		-23 ± 24	$+0.10 \pm 0.02$	$+0.01 \pm 0.05$
Twilights	G2V	-51 ± 2	-0.03 ± 0.002	$+0.01 \pm 0.002$

NOTE.—Differences in our stellar parameters from the averages of the values reported in Table 8. Deltas are Ours - Other. Twilight values are excluded from the average as the twilight spectra suffer from significantly higher scattered light and the small uncertainties would heavily bias the average. We note that the elevated $[\text{Fe}/\text{H}]$ is driven entirely by HIP 48331: excluding it $\Delta[\text{Fe}/\text{H}]$ becomes -0.03 ± 0.03 dex, consistent with our twilight values.

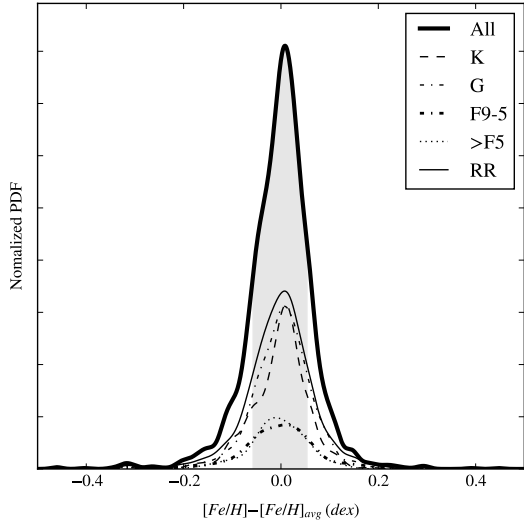


Fig. 10.— This plot shows normalized PDFs for $\Delta[\text{Fe}/\text{H}]$ for the entire sample as well as sub-samples based on spectral type and stars with $v_r \sin(i) > 8$ km/s (RR). The shaded region corresponds to 1σ for the entire sample.

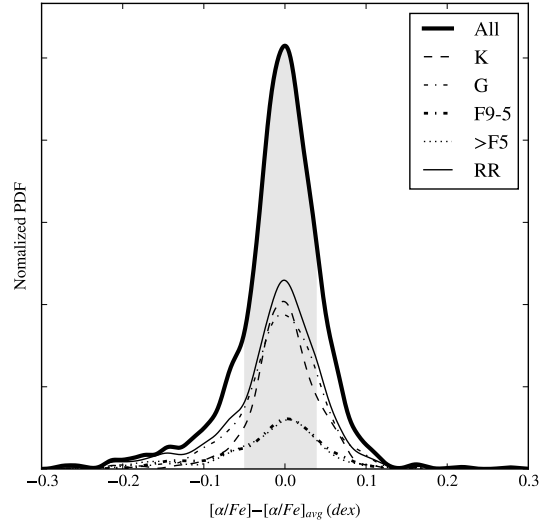


Fig. 11.— This plot shows normalized PDFs for $\Delta[\alpha/\text{Fe}]$ for the entire sample as well as sub-samples based on spectral type and stars with $v_r \sin(i) > 8$ km/s (RR). The shaded region corresponds to 1σ for the entire sample.

surement error, σ_{meas} ,

$$\sigma_{meas}^2 = \sigma_{phot}^2 + \sigma_{inst}^2 + \sigma_{anal}^2.$$

Here we focus on estimating σ_{meas} as a function of S/N, based on observations of the standard star HIP 48331.

We observed HIP 48331 35 times on 19 different nights; 9 nights have more than 1 epoch. Of these we use the 31 spectra with S/N above 200 and $R > 38,000$. Eighteen spectra were obtained using the red M2FS arm and 13 using the blue arm. The S/N of these spectra span between 200 and 300, with a median of 240. The resolving power of these spectra range from 40,000 to 64,000, with a median of 55,000 due to variations in the PSF width across the M2FS detector and soft instrument focus during early observing runs. The RV measurements of HIP 48331 are illustrated in Figure 13; these values have a standard deviation (σ_{obs}) of 23 m/s.

To simulate lower S/N spectra that are more representative of the open cluster stars surveyed here, we generated lower S/N versions of these 31 spectra and recomputed the best fit models and RVs from which new σ_{obs} can be calculated. We generated the the lower S/N spectra by sampling a Poisson process at each pixel with expectation value of the measured electrons multiplied by the desired fractional reduction in mean S/N: e. g.

$$x'_i = \text{Poisson}(sn'x_i/sn)$$

where x_i is the number of electrons measured at the i^{th} pixel and prime denotes the new values. We also ensured that the simulated variance spectra included in an appropriate amount of Gaussian noise to include the effects of detector read noise. The resulting spectra have S/N levels of $\sim 150, 100, 80, 60, 50, 40,$ and 15. The spectra were then fit as described in Section 4, treating each S/N level independently. This resulted in eight RV time-series (one for each S/N level) with each standard deviation yielding a measurement of σ_{obs} at that S/N level. We also computed σ_{phot} for each of the 248 spectra by applying the algorithm described in Butler et al. (1996) to the telluric and stellar components of each best-fit model, adding the results in quadrature.

To obtain σ_{meas} from the eight σ_{obs} values calculated above, we subtracted off a stellar variability of $\sigma_{stel} = 5.0$ m/s (Soubiran et al. 2013) and

an atmospheric variability of $\sigma_{atm} = 2.5$ m/s (determined as shown later in this section, see also Figure 18). These values can be compared directly to the the mean σ_{phot} values for each of the eight S/N bins. Oddly, we found that would result in imaginary errors below a S/N of ~ 60 . In Figure 14 we plot both σ_{meas} and σ_{phot} , which shows that we measure our RVs with greater precision that anticipated at low S/N. In Figure 14, we also show the ratio of σ_{meas} to the mean of σ_{phot} at each S/N bin. As an additional reference we also plot the ratio of each bin σ_{meas} to each of the σ_{phot} in that bin. This suggests an approximately linear relation between our measurement error and the σ_{phot} value we computed for each spectrum. We adopted errors for the ratio from two sources: (1) the standard deviation of σ_{phot} in each S/N bin contributes directly and (2) an estimate of the error in σ_{obs} that was obtained by computing our best-fit models with a small number of slightly perturbed initial RVs for each spectrum in each bin, adopting the standard deviations of the resulting σ_{obs} values as an uncertainty on σ_{meas} in each S/N bin.

We fit the ratio of σ_{meas} to the mean of the σ_{phot} for each S/N bin and use the result as a scaling relation to convert σ_{phot} to σ_{meas} provided a S/N. This technique allows us to account for some, if not all, of the increased uncertainty in spectra that are at a lower resolution (e.g. due to mis-focus) than the typical RV standard observation, are of more rapidly rotating stars, or otherwise possess a different number or strength of stellar lines. The errors in Figure 13 have been scaled in this manner.

From this analysis we find M2FS has a limiting RV precision of about 25 m/s, though the σ_{phot} values we computed at high S/N suggest an additional 15 m/s precision gain may be possible at higher S/N ratios. A potential culprit in our modeling process is as yet unclear. In Figures 15 and 16 we use the same process to show the impact various modifications to our analysis have on achievable precision, some of which are discussed in further detail in the following paragraphs. Finally, Figure 17 shows an updated version of Figure 3 with the corrections discussed above.

Atmospheric Variability We estimated the impact bulk atmospheric motions have on our

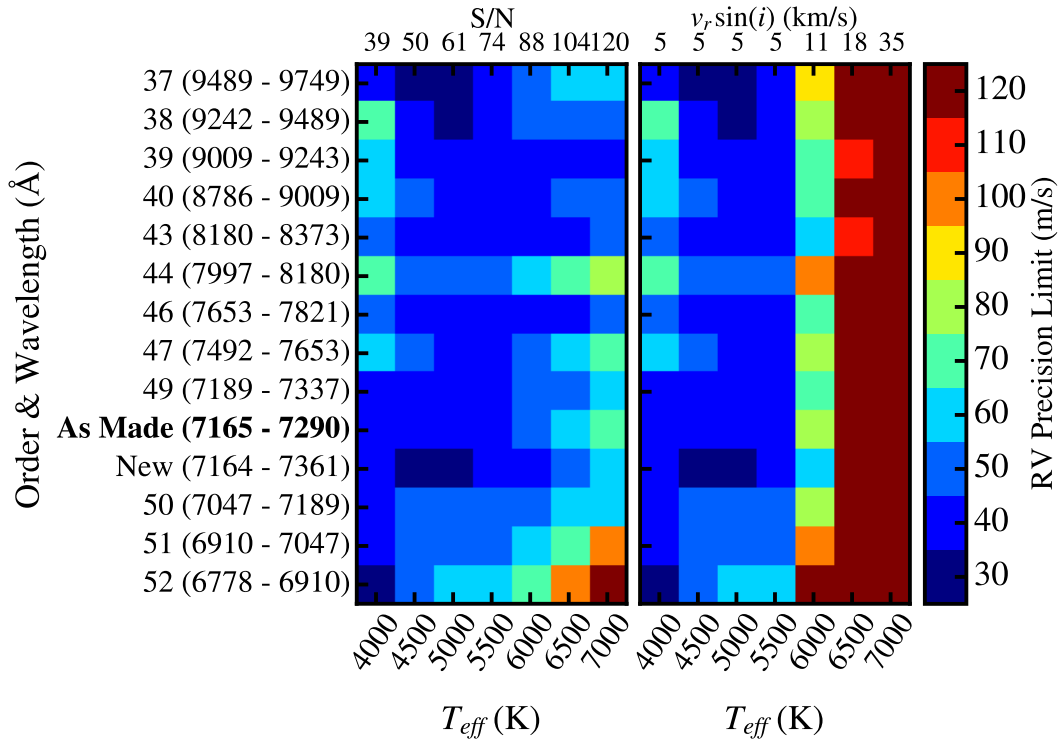


Fig. 17.— This is an updated version of Figure 3 where the algorithmic uncertainties have been corrected as described in Section 5.2.1. Both plots are at our median observed resolving power of 50,000. The S/N of each spectrum is determined by assuming equidistant MS dwarfs where a S/N of 50 is attained for a K5 dwarf. The resulting scale is marked at the top of the left plot, which assumes all stars have a $v_r \sin(i)$ of 5 km/s. The right plot uses the same S/N scale combined with the median $v_r \sin(i)$ values we measure for stars with the stated T_{eff} in NGC 2516 and NGC 2422. The right panel thus presents a worst case scenario for our technique as these clusters are some of the youngest suitable for precision RV work. In addition to standard M2FS orders we note the truncated order 49 used in this paper as “As Made” and our expectations for the new filter described in Section 2.2 as “New.”

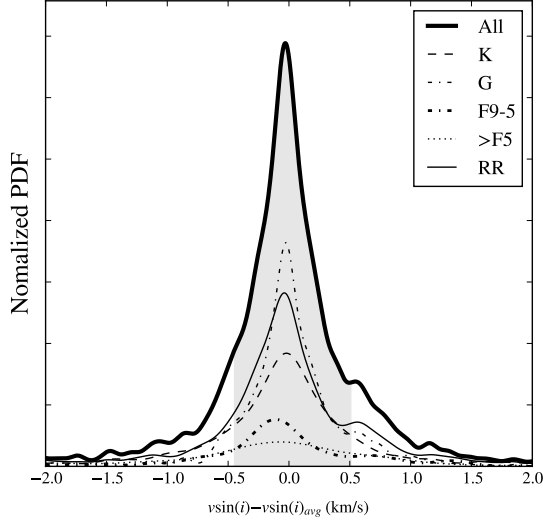


Fig. 12.— This plot shows normalized PDFs for $\Delta v_r \sin(i)$ for the entire sample as well as sub-samples based on spectral type and stars with $v_r \sin(i) > 8$ km/s (RR)..

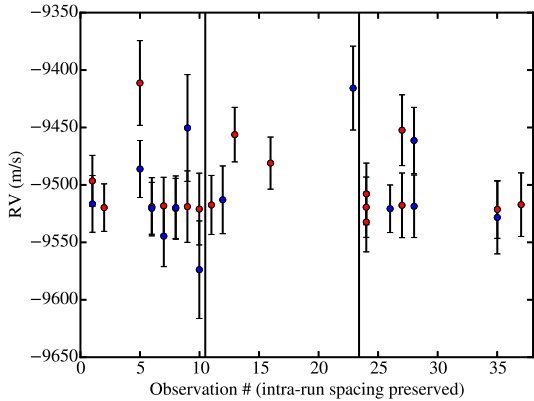


Fig. 13.— A plot of our measurements of HIP 48331. Points are colored by the arm used for the observation, in this regard these observations represent a more stringent test of M2FS’s stability than program stars which typically always use the same fiber and spectrographic channel.

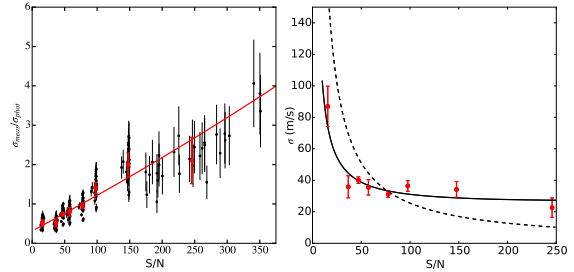


Fig. 14.— The left panel shows the ratio of σ_{meas} , computed from measurements of the RV standard at each resampled S/N step, to σ_{phot} , which is computed from the model of each spectrum. The individual points are each of the RV standard spectra and are provided for visual reference. We fit to the means at each S/N bin. Errors are as described in the text. The right, most dispersed group of points reflects the native S/N of observations of HIP 48331. The right panel shows σ_{meas} for each S/N bin along with an interpolated function generated using the fit in the left panel and the dashed curve. The dashed curve shows the mean of the σ_{phot} values computed using the models from fits to the high-S/N RV standard spectra with the calculation fed various S/N levels. This shows a clear indication that the algorithm overestimates uncertainty at low S/N. The plot also shows we are subject to a systematic floor of about 25 m/s

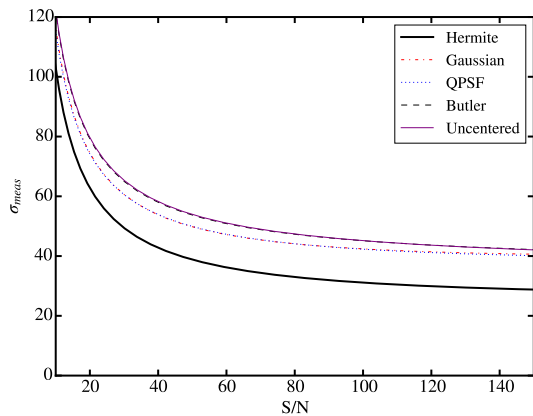


Fig. 15.— This plot shows the impact various PSF modeling choices have on σ_{meas} . The solid black line denotes σ_{meas} for our adopted analysis technique (c.f Fig 14). The red dash-dotted line corresponds to our analysis but using a simple, fixed Gaussian PSF. The blue dotted line – essentially on top of the red line – is for fits done using a Gaussian PSF with a FWHM as described by a quadratic. The thin, dashed black line and the thin purple line – also nearly superimposed – correspond to fits done with the PSF prescription of Butler et al. (1996) and our adopted, Hermite prescription but without the enclosed power constrained to the central pixel.

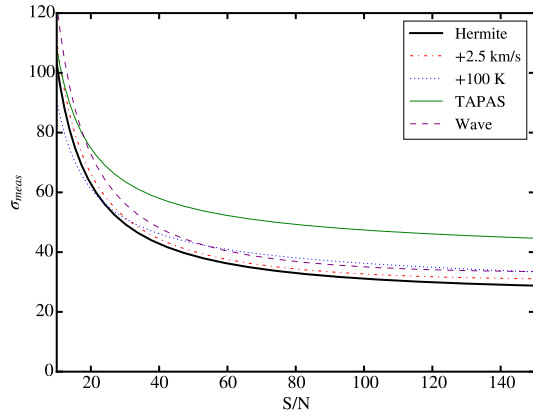


Fig. 16.— This plot shows the impact of various factors on our attained RV measurement precision. The solid black line denotes σ_{meas} for our adopted analysis technique (c.f Fig 14). The red dash-dotted line corresponds to a fits done with a $v_r \sin(i)$ 2.5 km/s larger than the optimal value. The blue dotted line corresponds to fits done with T_{eff} forced 100 K above our adopted value. The purple dashed line is for fits done without holding the 4th and higher order wavelength parameters fixed as described in Section 4.2.3. Finally, the solid green line represents our results when we use the TAPAS synthetic telluric spectra as our wavelength reference instead of the NSO empiric spectrum.

wavelength reference by integrating the water vapor weighted wind speed along the line of sight using data from the NOAA GFS forecast models (NCEP 2003). Using the GFS model closest in time to our data the forecast is within 3 hours of the model’s initial conditions. These models have an RMSE wind vector error of about 3 m/s three days (!) in the future. Perturbing the integrals by this error has a maximum impact of about 1 m/s, with typical values less than a tenth of that. The resulting contributions for our data on HIP 48331, NGC 2516, and NGC 2422 are shown in Figure 18. While pointing directly into or along the jet-stream would exhibit a clear signature at the ± 5 m/s level, typical values are not particularly significant to our efforts. As mentioned, we adopt $\sigma_{atm} = 2.5$ m/s.

Sky Emission Ideally the spectra we obtained of our RV standard would be completely representative of our program stars. Our cluster targets are, however, significantly fainter than our RV standard and so many of them exhibit a number of strong sky emission lines (c.f. Figure 6 and 8). To better assess their impact on our RV precision we took a subset of 60 spectra and extracted and fit the spectra from images prior to stacking. This gave us a sample of 4 or 5 RVs from spectra obtained consecutively. These spectra spanned a S/N of about 15 – 45 for targets of spectral type \sim K3 - F5. The σ_{obs} for these RVs was in agreement with that expected based on our σ_{meas} relation. We see some evidence that our better-than-anticipated RV precision stems from our use of the mean RV as a prior. If fit with an initial RV far from the multi-epoch mean we observe an increased σ_{obs} at low S/N, though still somewhat below that predicted by Butler et al. (1996, c.f. Figure 14).

PSF effects We found very little difference in the results of the multi-Gaussian parameterization of Butler et al. (1996) and a Gauss-Hermite kernel when the center of its enclosed power is not constrained to the central pixel undergoing convolution. The latter is faster with many fewer parameters and once the enclosed power is constrained to the central sub-pixel we find it exhibits enhanced stability (c.f. Figure 15). Both yielded slightly worse performance than a simple Gaussian and

we did not find an improvement in RV precision by using a variable, but symmetric PSF. It may be worth investigating a hybrid approach where the components of the Hermite parametrization are allowed to vary with pixel.

Model Spectra As an additional test on RV precision and the impact our use of the PHOENIX grid has we model the twilight spectra both with the PHOENIX grid and using the empiric Solar spectrum of Kurucz (2005) as the template. We select the \sim 600 twilight spectra in images with mean S/N above 100 (100 – 650, mean of 320). For these spectra we measured a 1σ RV scatter within each twilight image of 23 ± 1.4 m/s when fitting with the PHOENIX models and 28 ± 2.3 m/s using Kurucz’s empiric Solar spectra. This strongly suggests that the PHOENIX templates are not limiting our RV precision. We see evidence of a slight quadratic dependence of the measured RV on the spectrum’s CCD position. This suggests that the RV zero point and wavelength zero points are slightly affecting our dispersion, though we note that program stars are typically observed in the same fiber. Fitting and removing this effect reduced the scatter to 18 ± 1.2 m/s and 23 ± 2.3 m/s, respectively.

5.2.2. Accuracy

We estimated the accuracy of our RVs by looking at the differences between our values and those in the literature for each of our six standard stars. We report these differences in Table 10 and find an offset of 74 ± 72 m/s from the scale of Soubiran et al. (2013), albeit with significant scatter. We also saw a slight indication that RVs measured in our lowest S/N bin are slightly shifted relative to the higher S/N bins by 27 ± 17 m/s.

6. Discussion

Given M2FS’s unique ability to efficiently obtain precision optical spectra capable of determining accurate stellar properties and precision RVs, here we briefly summarize the broader scientific impact this instrument could have for both finding exoplanets in open clusters and improving our understanding of the stars in these clusters.

TABLE 10
STANDARD RV DIFFERENCES

Target	Type	N	ΔRV (m/s)
HIP 48331	K5V	30	2 ± 7
HIP 13388	K1V	2	41 ± 40
HIP 10798	G8V	5	139 ± 7
HIP 22278	G5V	3	173 ± 17
HIP 19589	G0V	1	-77 ± 94
HIP 31415	F6V	1	173 ± 78
Average			74 ± 72

NOTE.—Differences in our RVs compared to the values reported in Table 3. Differences are Ours - Other.

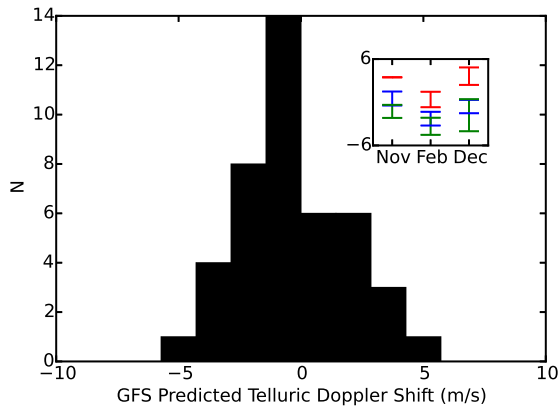


Fig. 18.— A histogram of the telluric atmosphere imposed RV shifts to observations of HIP 48331, NGC 2516, and NGC 2422. The standard deviation about zero is 2.3 m/s. The inset shows the means and standard deviations from our November 2013, February 2014, and December 2014 observing runs for the three sets of targets separately in green, blue, and red respectively.

6.1. M2FS as a Tool for Finding Planets in Open Clusters

Though once unexpected, it is now clear that a great many hot-gas giants exist. Assuming 1.2% of F5-K5 stars in open clusters harbor hot gas planets ($P < 10$ days, $M \sin(i) > 0.1 M_{\text{Jup}}$) (Wright et al. 2012; Meibom et al. 2013) and given our achieved precision we can predict the limits of our technique. For example, we expect M2FS will be capable of attaining a S/N 25 spectrum of a K5V star at a DM of 9.5 in 4 hours (effectively 2 minutes per star). This would be sufficient for an RV precision of ~ 55 m/s, with brighter members increasingly limited by the systematics in our analysis. In this hypothetical cluster we would then be sensitive to $\sim 75\%$ of known hot gas giants. Figure 19 shows our anticipated RV measurement precision as a function of distance modulus using the new filter. This implies we could reasonably expect one Hot-Jupiter per M2FS pointing, provided targets are available for the majority of fibers.

Table 11 lists the eight nearby open clusters that matched the cluster selection criteria given in Section 2.1. From these clusters we can obtain ~ 15 M2FS pointings and would expect about as many exoplanet candidates. We highlight that these clusters span a range of ages and are thus well suited to help build a sample of exoplanets

that addresses the formation and migration issues discussed in the introduction.

This program would also well characterize the Doppler uncertainty commonly referred to as stellar jitter as a function of age. This issue is not yet well constrained (c.f. Mahmud et al. 2011; Lagrange et al. 2013) and the present state of our knowledge is largely summarized in Figure 20, which shows the stellar jitter as a function of age for a young association and two open clusters along with the ages of open clusters our expanded survey will target. Extant data is far from homogenous – a mix of both optical and infrared spectroscopy – and suffers from rather small sample sizes. By surveying a large number of stars in clusters over a range of ages we will well constrain this effect with age and determine what truly constitutes “too young” to measure precision RVs.

We note that M2FS’s strength is in identification: though the ability to survey large numbers of stars at this precision is unmatched, we would suggest that followup of promising candidates is better suited to traditional monitoring programs.

6.2. M2FS as a Tool for Studying Open Cluster Stellar Populations

The success of any large scale RV survey of open clusters for planets depends critically on having a carefully vetted sample to survey. M2FS is poised to do this. First, precision RVs will help confirm membership, especially when combined with Gaia proper motions. Second, precision RVs can identify spectroscopic binaries that are typically poor targets for exoplanet searches. Finally, the high dispersion spectra allow measures of $v_r \sin(i)$, T_{eff} , and metallicity, with the latter two yielding stellar masses from evolutionary models. When coupled with photometric periods determined by LSST, we could even determine stellar inclinations and identify edge-on systems. The flexible nature of M2FS also means that we could also obtain spectra of the Ca II H and K region for all of our targets with a relatively modest overhead (~ 20 min total for targets in NGC 2516 and NGC 2422), further helping calibrate stellar ages.

A number of recent papers have also highlighted the importance both stellar multiplicity and metallicity play in star formation and have drawn attention to various gaps in current simu-

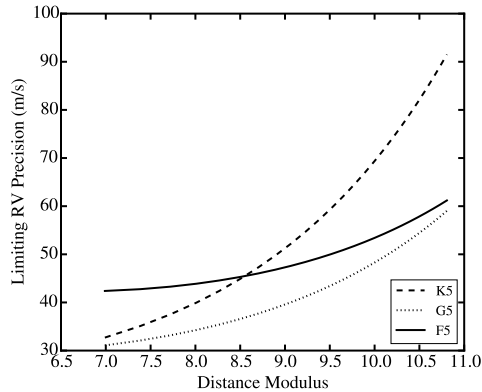


Fig. 19.— A plot of anticipated RV precision for quiescent, slowly-rotating K5, G5, and F5 stars as function of distance modulus after 2.5 hours observing in one arc second seeing with the corrected filter.

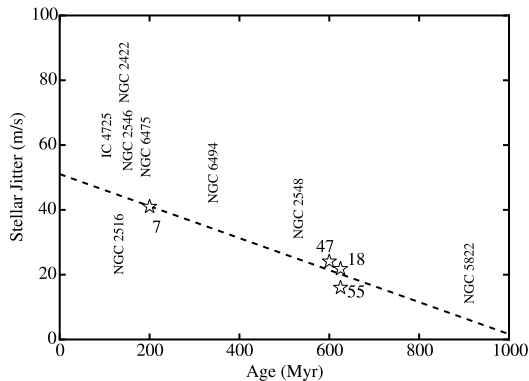


Fig. 20.— A plot of the literature values for stellar jitter as a function of age. Sample sizes are noted by each point. The dashed line is a simple, linear fit to guide the eye. The various clusters well matched to M2FS’s grasp are noted at their approximate ages. Data is from Paulson & Yelda (2006); Paulson et al. (2004); Quinn et al. (2012, 2014).

lations of cluster evolution (Paunzen et al. 2010; Geller et al. 2010; Duchêne et al. 2007). Our stellar properties directly address such gaps by characterizing the cluster chemical environment while our RVs allow robust identification of binaries and brown dwarfs (constrained by our time baseline), characterizing the kinematic environment. Such a dataset can contribute to the initial conditions used in dynamical simulations of cluster formation.

We also note there is an absence of precision internal kinematics for open clusters. This dataset is useful to study the internal dynamics of open clusters at the 10 m/s level. With an anticipated precision of better than 10 μ as/yr (~ 20 m/s at 500 pc) (Lindegren 2010; Lindegren et al. 2012), once GAIA data is available for our targets the combined dataset will offer an unprecedented 3D kinematic picture of stars within open clusters, providing a useful tool to study internal kinematics.

7. Summary

We have presented a program to use the Michigan/Magellan Fiber System to obtain multiplexed spectroscopy of solar analog stars in nearby (<1 kpc) open clusters with the intent of identifying exoplanet host stars for subsequent followup. Our technique uses telluric lines in the 7230 Å region as a wavelength reference and is presently capable of measuring RVs with a precision of 25-60 m/s, depending on S/N. We also obtain precise and accurate measurements of T_{eff} , $[Fe/H]$, $[\alpha/Fe]$, and $v_r \sin(i)$ for all of our target stars thereby enabling characterization of the cluster environment. This paper is the first in a series of papers on our efforts and described our analysis procedure in detail. The next paper in this series will report the RVs and stellar parameters of targets in NGC 2422 and NGC 2516 and carry out an analysis of the companion detectability therein. Later papers will use our sample to study binaries in our sample and analyze emergent cluster properties.

The authors gratefully acknowledge valuable discussions with Sam Quinn, Peter Gao, Justin Cantrell, and Colin Slater. J.B. and M.M. acknowledge support from NSF AAG grant 1312997 and the NFS/MRI development grant 0923160.

R.W. acknowledges support from NSF AAG grant 1009634 and NASA Origins of Solar Systems grant NNX11AC32G. PyRAF is a product of the Space Telescope Science Institute, which is operated by AURA for NASA. This research made use of Astropy, a community-developed core Python package for Astronomy (Astropy Collaboration, 2013).

Facilities: Magellan:Clay(M2FS)

REFERENCES

- Ciardi, D. R., van Eyken, J. C., Barnes, J. W., et al. 2015, ApJ, 809, 42
- Crockett, C. J., Mahmud, N. I., Prato, L., et al. 2012, ApJ, 761, 164
- Huerta, M., Johns-Krull, C. M., Prato, L., Hartigan, P., & Jaffe, D. T. 2008, ApJ, 678, 472
- Huélamo, N., Figueira, P., Bonfils, X., et al. 2008, A&A, 489, L9
- Prato, L., Huerta, M., Johns-Krull, C. M., et al. 2008, ApJ, 687, L103
- Meynet, G., Mermilliod, J.-C., & Maeder, A. 1993, A&AS, 98, 477
- Loktin, A. V., Gerasimenko, T. P., & Malysheva, L. K. 2001, Astronomical and Astrophysical Transactions, 20, 607
- Sung, H., Bessell, M. S., Lee, B.-W. & Lee, S.-G. 2002, AJ, 123, 290
- Cochran, W. D. 1988, ApJ, 334, 349
- Crockett, C. J., Mahmud, N. I., Prato, L., et al. 2011, ApJ, 735, 78
- Figueira, P., Pepe, F., Lovis, C., & Mayor, M. 2010, A&A, 515, A106
- Blake, C. H., Charbonneau, D., White, R. J., Marley, M. S., & Saumon, D. 2007, ApJ, 666, 1198
- Blake, C. H., Charbonneau, D., & White, R. J. 2010, ApJ, 723, 684
- Seifahrt, A., Käufel, H. U., Zängl, G., et al. 2010, The Messenger, 142, 21
- Gao, P., Plavchan, P., Gagne, J., et al. 2015, American Astronomical Society Meeting Abstracts, 225, 258.22

TABLE 11
POTENTIAL TARGET CLUSTERS

Cluster	Age (Myr)	Distance (pc)	R_{Cen} (deg)	[Fe/H]	$\sim N_{Targ}$
IC 4725 (M25)	93	560	0.5	-0.3	100
NGC 2546	140	930	0.8	+0.12	200
NGC 6475 (M 7)	180	300	0.8	+0.14	150
NGC 6494	330	650	0.5	+0.09	200
NGC 2548	520	790	1.1	+0.08	100
NGC 5822	900	800	0.5	-0.02	500
NGC 2422 (M 47)	132	491	0.3	+0.02	160
NGC 2516	120	346	0.4	-0.18	330

NOTE.—The numbers given for NGC 2516 and NGC 2422 are in addition to those already observed. R_{Cen} refers to the approximate half-light radius of the clusters, while N_{Targ} is the approximate number of members available near the cluster centers within the field of view of M2FS.

- Mayor, M., Pepe, F., Queloz, D., et al. 2003, *The Messenger*, 114, 20
- Ge, J., Mahadevan, S., Lee, B., et al. 2008, *Extreme Solar Systems*, 398, 449
- Tody, D. 1993, *Astronomical Data Analysis Software and Systems II*, 52, 173
- Adams, F. C., & Laughlin, G. 2006, *ApJ*, 649, 1004
- Adibekyan, V. Z., Sousa, S. G., Santos, N. C., et al. 2012, *A&A*, 545, A32
- Bailey, J. I. I., White, R. J., Blake, C. H., et al. 2012, *ApJ*, 749, 16
- Bailey, J. I., Mateo, M. L., Bagish, A. P., Crane, J. D. & Slater, C. T. in (McLean, I. S., Ramsay, S. K. & Takami, H.) *SPIE, 2012, SPIE Astronomical Telescopes + Instrumentation*, 8446, 84465G
- Bean, J. L., Seifahrt, A., Hartman, H., et al. 2010, *ApJ*, 713, 410
- Bertaux, J. L., Lallement, R., Ferron, S., Boonne, C. & Bodichon, R. 2014, *A&A*, 564, 46
- Boss, A. P. 1997, *Science*, 276, 1836
- Brucalassi, A., Pasquini, L., Saglia, R., et al. 2014, *A&A*, 561, L9
- Butler, R. P., Marcy, G. W., Williams, E., et al. 1996, *PASP*, 108, 500
- Casagrande, L., Ramírez, I., Meléndez, J., Bessell, M. & Asplund, M. 2010, *A&A*, 512, 54
- Casagrande, L., Schoenrich, R., Asplund, M., et al. 2011, *A&A*, 530, A138
- Charbonneau, D., Brown, T. M., Burrows, A., & Laughlin, G. 2007, *Protostars and Planets V*, 701
- Ciddor, P. E. 1996, *Applied Optics LP*, 35, 1566
- Coelho, P. R. T. 2014, *MNRAS*, 440, 1027
- Cochran, W. D. 1988, *ApJ*, 334, 349
- de Laverny, P., Recio-Blanco, A., Worley, C. C., & Plez, B. 2012, *A&A*, 544, A126
- Duchêne, G., Delgado-Donate, E., Haisch, K. E., Jr., Loinard, L., & Rodríguez, L. F. 2007, *Protostars and Planets V*, 379
- Eastman, J., Gaudi, B. S., & Agol, E. 2013, *PASP*, 125, 83

- Edlén, B. 1966, *Metrologia*, 2, 71
- Fabrycky, D., & Tremaine, S. 2007, *ApJ*, 669, 1298
- Fortney, J. J., & Nettelmann, N. 2010, *Space Sci. Rev.*, 152, 423
- Fortney, J. J., Marley, M. S., Saumon, D., & Lodders, K. 2008, *ApJ*, 683, 1104
- Galvagni, M., Hayfield, T., Boley, A., et al. 2012, *MNRAS*, 427, 1725
- Geller, A. M., Mathieu, R. D., Braden, E. K., et al. 2010, *AJ*, 139, 1383
- Głębocki, R., & Gnaniński, P. 2005, 13th Cambridge Workshop on Cool Stars, Stellar Systems and the Sun, 560, 571
- Goldreich, P. & Tremaine, S. 1980, *ApJ*, 241, 425
- Gray, D. F. 1992, *Camb. Astrophys. Ser.*, Vol. 20
- Griffin, R., & Griffin, R. 1973, *MNRAS*, 162, 255
- Helled, R., Bodenheimer, P., Podolak, M., et al. 2014, *Protostars and Planets VI*, 643
- Howell, S. B., Sobek, C., Haas, M., et al. 2014, *PASP*, 126, 398
- Hubeny, I. & Lanz, T. 2011, *ascl soft*, 09022
- Husser, T. O., Wende-von Berg, S., Dreizler, S., et al. 2013, *A&A*, 553, A6
- Jeffries, R. D., Thurston, M. R. & Hambly, N. C. 2001, *A&A*, 375, 863
- Jones, A., Noll, S., Kausch, W., Szyszka, C., & Kimeswenger, S. 2013, *A&A*, 560, A91
- Jurić, M., & Tremaine, S. 2008, *ApJ*, 686, 603
- Kharchenko, N. V., Piskunov, A. E., Röser, S., Schilbach, E. & Scholz, R. D. 2005, *A&A*, 438, 1163
- Kordopatis, G., Gilmore, G., Steinmetz, M., et al. 2013, *AJ*, 146, 134
- Kurucz, R. L. 2005, *Memorie della Societa Astronomica Italiana Supplementi*, 8, 189
- Lagrange, A.-M., Meunier, N., Chauvin, G., et al. 2013, *A&A*, 559, A83
- Lin, D. N. C., Bodenheimer, P., & Richardson, D. C. 1996, *Nature*, 380, 606
- Lindgren, L. 2010, *IAUS*, 261, 296
- Lindgren, L., Lammers, U., Hobbs, D., O'Mullane, W., Bastian, U., Hernandez, J. 2012, *A&A*, 538, 78
- Mahmud, N. I., Crockett, C. J., Johns-Krull, C. M., et al. 2011, *ApJ*, 736, 123
- Markwardt, C. B. 2009, *Astronomical Data Analysis Software and Systems XVIII*, 411, 251
- Marley, M. S., Fortney, J., Seager, S., & Barman, T. 2007, *Protostars and Planets V*, 733
- Mateo, M., Bailey, J. I., Crane, J., et al. in (McLean, I. S., Ramsay, S. K. & Takami, H.) *SPIE*, 2012, *SPIE Astronomical Telescopes + Instrumentation*, 8446, 84464Y–84464Y–19
- Meibom, S., Torres, G., Fressin, F., et al. 2013, *Nature*, 499, 55
- Mizuno, H. 1980, *PThPh*, 64, 544
- Mordasini, C., Alibert, Y., Klahr, H., & Henning, T. 2012, *A&A*, 547, A111
- Environmental Modeling Center, 2003: *The GFS Atmospheric Model*. NCEP Office Note 442, Global Climate and Weather Modeling Branch, EMC, Camp Springs, Maryland.
- Nelder, J. A. & Mead, R. 1965, *Computer Journal*, 7, 308
- Neves, V., Santos, N. C., Sousa, S. G., Correia, A. C. M., & Israelian, G. 2009, *A&A*, 497, 563
- Noll, S., Kausch, W., Barden, M., et al. 2012, *A&A*, 543, A92
- Paulson, D. B., Cochran, W. D., & Hatzes, A. P. 2004, *AJ*, 127, 3579
- Paulson, D. B. & Yelda, S. 2006, *PASP*, 118, 706
- Paunzen, E., Heiter, U., Netopil, M., & Soubiran, C. 2010, *A&A*, 517, A32
- Pepe, F., Lovis, C., Ségransan, D., et al. 2011, *A&A*, 534, A58

- Prisinzano, L., Micela, G., Sciortino, S. & Favata, F. 2003, A&A, 404, 927
- Quinn, S. N., White, R. J., Latham, D. W., et al. 2012, ApJ, 756, L33
- Quinn, S. N., White, R. J., Latham, D. W., et al. 2014, ApJ, 787, 27
- Rasio, F. A., & Ford, E. B. 1996, Science, 274, 954
- Ribas, I. 2010, Proc. IAU, 5, 3
- Rothman, Gordon, Barbe, et al. 2009, J. Quant. Spec. Radiat. Transf., 110, 533
- Santos N. C., Israelian G., Mayor M., et al. 2005, A&A, 437, 1127
- Seifahrt, A., Käufel, H. U., Zängl, G., et al. 2010, The Messenger, 142, 21
- Soubiran, C., Jasiewicz, G., Chemin, L., et al. 2013, A&A, 552, 64
- Sousa, S. G., Santos, N. C., Mayor, M., et al. 2008, A&A, 487, 373
- Sung, H., Bessell, M. S., Lee, B.-W. & Lee, S.-G. 2002, AJ, 123, 290
- Terndrup, D. M., Pinsonneault, M., Jeffries, R. D., et al. 2002, ApJ, 576, 950
- Tsantaki, M., Sousa, S. G., Adibekyan, V. Z., et al. 2013, A&A, 555, A150
- Valenti, J. A., & Fischer, D. A. 2005, ApJS, 159, 141
- van Dokkum, P. G. 2001, PASP, 113, 1420
- Wallace, L., Hinkle, K. H., Livingston, W. C. & Davis, S. P. 2011, ApJS, 195, 6
- Wright, J. T., Marcy, G. W., Howard, A. W., et al. 2012, ApJ, 753, 160
- Zacharias, N., Finch, C. T., Girard, T. M., et al. 2013, AJ, 145, 44